Wear 601 (2026) 206842

Contents lists available at ScienceDirect

Wear

journal homepage: www.elsevier.com/locate/wear

Mechanisms of wheel wear evolution and wheel-rail contact geometry variation in locomotives

Hu Li [a,b], Yuan Yao [a,*], Zhiyong Shi [b], Enrico Meli [b], Xiaoxing Deng [a,c], Jijun Gong [a,d], Guang Li [e]

[a] *State Key Laboratory of Rail Transit Vehicle System, Southwest Jiaotong University, Chengdu, 610031, China*
[b] *Department of Industrial Engineering, University of Florence, Firenze, 50139, Italy*
[c] *Bogie R&D Department, CRRC Zhuzhou Electric Locomotive Co., Ltd., Zhuzhou, 412001, China*
[d] *China Railway Materials Operation and Maintenance Technology Co.,Ltd., Beijing, 100036, China*
[e] *Metals & Chemistry Research Institute, China Academy of Railway Sciences Co. Ltd., Beijing, 100081, China*

ARTICLE INFO

Keywords:
Power-concentrated trainset
Wheel wear
Equivalent conicity
Wheel-rail maintenance

ABSTRACT

Abnormal wheel-rail wear frequently leads to deteriorated dynamic behaviour in power-concentrated trainsets. These problems originate from changes in wheel-rail contact geometry, which can be effectively characterized by equivalent conicity. This study investigates wheel wear evolution mechanism and its influencing factors in terms of wear depth and nominal wear-peak migration. Two locomotive-type power heads used in power-concentrated trainsets are examined: an in-service B-type locomotive equipped with two-axle bogies and a C-type locomotive under testing equipped with three-axle bogies. Long-term field measurements were first used to define the nominal wear-peak position and classify wear types. A multibody dynamics model and a wheel wear prediction model were then established and validated using measured worn profiles. Simulation analyses identified rail profile, rail inclination, operating speed, and axle torque as the dominant factors. For C-type locomotives, the evolution of equivalent conicity is primarily affected by the lateral migration of the nominal wear peak position rather than wear depth; increasing the percentage of CN60 rail, increasing operating speed, and reducing axle torque effectively suppress conicity growth. Consequently, wheel reprofiling intervals for the C-type locomotive may be extended if equivalent conicity remains within allowable limits, thereby reducing maintenance frequency and improving wheel life. In contrast, the equivalent conicity of B-type locomotives shows limited sensitivity to wear-peak migration, suggesting that should focus mainly on target wear depth control. This study reveals the mechanisms by which wear depth and wear distribution jointly affect equivalent conicity evolution and translates these insights into operation-oriented, condition-based maintenance recommendations for power-concentrated trainsets.

1. Introduction

Wheel-rail contact geometry plays a crucial role in determining the dynamic behaviour of rail vehicles. As wheel and rail wear progressively develop during service, the geometric relationship at the wheel-rail contact interface is continuously altered, which may lead to the degradation of vehicle dynamic behaviour. Given the critical influence of wheel-rail contact conditions on operational safety, wheel-rail wear has long been a major research focus in the railway field [1–6]. Wheel-rail contact geometry determines the rolling radii difference function $\Delta r(y)$, which describes the difference of the current rolling radii of the two wheels as a function of the wheelset's current lateral displacement y. The rolling radius difference provides the basis for the guidance and self-centering ability of the wheelset. Thereby, the wheel-rail contact geometry has a strong impact on the dynamic behaviour of the vehicle, in particular its lateral dynamic behaviour, which includes the hunting behaviour and the running stability. The rolling radii difference function $\Delta r(y)$ is commonly characterized by the equivalent conicity. Combining these two aspects, the equivalent conicity is a useful indicator for the current running behaviour of the vehicle. Both excessively high and excessively low equivalent conicity values may adversely affect vehicle dynamic behaviour. For a relatively low equivalent conicity,

* Corresponding author.
E-mail address: yyuan8848@163.com (Y. Yao).

https://doi.org/10.1016/j.wear.2026.206842
Received 12 January 2026; Received in revised form 2 June 2026; Accepted 5 June 2026
Available online 6 June 2026

low-frequency lateral motions of the entire vehicle including the carbody can occur, which deteriorates the ride comfort. An excessively high equivalent conicity leads to a hunting motion at higher frequencies, resulting in an increased lateral acceleration of the wheelset and higher lateral wheel-rail forces, which can cause damage to the track. Consequently, wheel-rail maintenance strategies are largely aimed at keeping equivalent conicity within an appropriate range to ensure that the vehicle's dynamic behaviour meets operational requirements.

To address wheel-rail wear and its impact on vehicle dynamic behaviour, extensive research has been devoted to wheel-rail wear prediction, with most studies focusing on the trade-off between prediction accuracy and computational efficiency [7–9]. Promising results have been reported using look-up table-based approaches [10] [11] and neural network models for wear prediction [12–14]. Other studies have examined the impact of wheel-rail wear on vehicle dynamic stability, providing deeper insights into the coupling mechanisms between wear evolution and vehicle dynamics [15–17]. In recent years, improving wear behaviour and running stability through wheel-rail profile optimization [18–20], suspension parameter tuning [21–23], and the adoption of advanced damping devices [24] [25] has emerged as a major research trend, with some methods already implemented in engineering practice. Collectively, these studies have significantly contributed to mitigating wear-related issues and have drawn increasing attention to the fundamental mechanisms affecting wheel-rail wear development [26].

Despite these advances, two limitations remain. First, wheel wear has been predominantly evaluated by wear depth. In the present work, the investigated vehicles operate on a high-speed line with relatively wide curves. Under such conditions, flange contact is unlikely, and wheel wear mainly develops on the tread. However, under such tread-wear-dominated conditions, the wear distribution along the wheel tread directly affects the evolution of the profile's shape, i.e., a strongly non-uniformly distributed wear will strongly change the profile, which in turn alters the contact geometry and thereby the rolling radii difference function and the vehicle's dynamic behaviour. Yet, this aspect has received relatively limited attention. Second, most existing investigations focus on metro vehicles and high-speed trainsets with distributed traction (electric multiple units or EMUs), whereas wheel wear evolution in power-concentrated trainsets has been far less studied. Since the introduction of power-concentrated trainsets in China, undesirable vibration phenomena such as low-frequency carbody shaking and high-frequency bogie vibrations have been frequently reported, largely associated with unfavourable wheel-rail contact geometries, which result from wear evolution. Against this background, the present study investigates wheel wear evolution mechanisms and their affecting factors, with particular emphasis on wear distribution and its implications for equivalent conicity. Two locomotive-type power heads used in power-concentrated trainsets are considered. For brevity, they are hereafter referred to as the B-type locomotive and the C-type locomotive.

Usually, the wear of the wheels is progressing faster than the wear of the rails. As a consequence, wheels have to be maintained much more frequently than rails, and changes of the rail profiles due to wear are negligible within a wheel reprofiling cycle. Therefore, this study focuses on the evolution of the wheel wear. It is well recognized that strongly non-uniformly distributed wear can significantly alter the shape of the wheel profile, which in turn affects the contact geometry and thereby the dynamic running behaviour of the vehicle. If this kind of wear also progresses more rapidly, shorter maintenance intervals become necessary in order to ensure an acceptable dynamic behaviour of the vehicle [27–30]. However, wheel wear should not be regarded as inherently detrimental. In some cases, pursuing a reduction in wheel wear at any cost is not necessarily desirable, since a low wear level may increase the risk of rolling contact fatigue (RCF) under certain wheel-rail contact conditions [31]. Moderate wheel wear generally has a limited influence on equivalent conicity and may even contribute to maintaining vehicle dynamic behaviour within a stable operating range. Several studies have reported that certain carbody shaking phenomena observed with new wheels tend to diminish once the wheels have experienced an initial wear-in period [32] [33]. Accordingly, many commonly used wheel profiles, such as the LM profile for metro vehicles and freight wagons, the S1002 profile for high-speed electric multiple units (EMUs), and the JM3 profile for locomotives, are designed as wear-adapted treads. In conventional wheel-rail maintenance practices, wheel reprofiling is typically scheduled once the accumulated mileage or wear depth reaches a predefined threshold to ensure operational safety. However, the ultimate purpose of wheel maintenance is to maintain favourable wheel-rail contact geometry, which ensures good dynamic running behaviour and which is characterized by an appropriate level of equivalent conicity. In practice, equivalent conicity does not necessarily exceed its allowable range when these mileage- or wear-based thresholds are reached. Therefore, in a maintenance strategy purely based on mileage or wear depth, wheel reprofiling may be carried out prematurely. This leads to increased costs not only due to the premature maintenance actions themselves, for which the vehicle has to be taken out of service, but also due to the reduction of the wheel's service life, since reprofiling is typically carried out by removing material and therefore cannot be repeated arbitrarily often. This possible mismatch between mileage- or wear-based maintenance criteria and dynamic behaviour indicators motivates the present study to investigate the evolution of equivalent conicity induced by wheel wear.

Given that wheel wear is influenced by a wide range of operational, vehicle structural characteristics, and contact-related factors, identifying the principal factors affecting wear evolution is essential for improving the reliability of wear prediction models. By systematically analyzing key contributors to tread wear under high-speed operating conditions with predominantly tread contact, and elucidating their mechanisms, this study aims to provide guidance for maintaining appropriate equivalent conicity and intelligent wheel-rail health management.

The structure of this paper is organized as follows. Section 2 presents the wheel wear tests and analyzes the experimental results, summarizing the tread-wear characteristics and classifying the wear types. Section 3 provides an overview of the vehicle dynamic simulation model and details the development and validation of the wheel wear prediction model. Section 4 presents simulation-based analyses aimed at identifying the key factors that drive wheel wear evolution; using iterative wear prediction, it further reveals their underlying influence mechanisms and proposes appropriate operation and maintenance strategies.

2. Wheel wear tracking test

The primary objective of the wheel wear tracking test is to systematically collect and analyze wheel wear data during locomotive operation, categorize the wear characteristics and types of wheel wear, and understand the impact mechanisms of wheel wear characteristics on wheel-rail contact geometry.

2.1. Overview of the wheel wear tracking test procedure

This study involved long-term monitoring of the wheel profiles of Type B locomotives in service. These locomotives, which serve as the power units for 160 km/h power-concentrated trainsets, have been progressively deployed for passenger services across various railway administrations in China since early 2019. All the Type B locomotives tested in this study were equipped with JM3 tread profiles after economic re-profiling. Unless otherwise specified, this profile was taken as the reference or initial wheel profile in the subsequent contact-geometry analyses. In economic reprofiling, the tread is preferentially restored toward its original profile because it is more relevant to high-speed dynamic behaviour, whereas limited flange deviations from the standard profile are allowed within the specified tolerances. As illustrated in

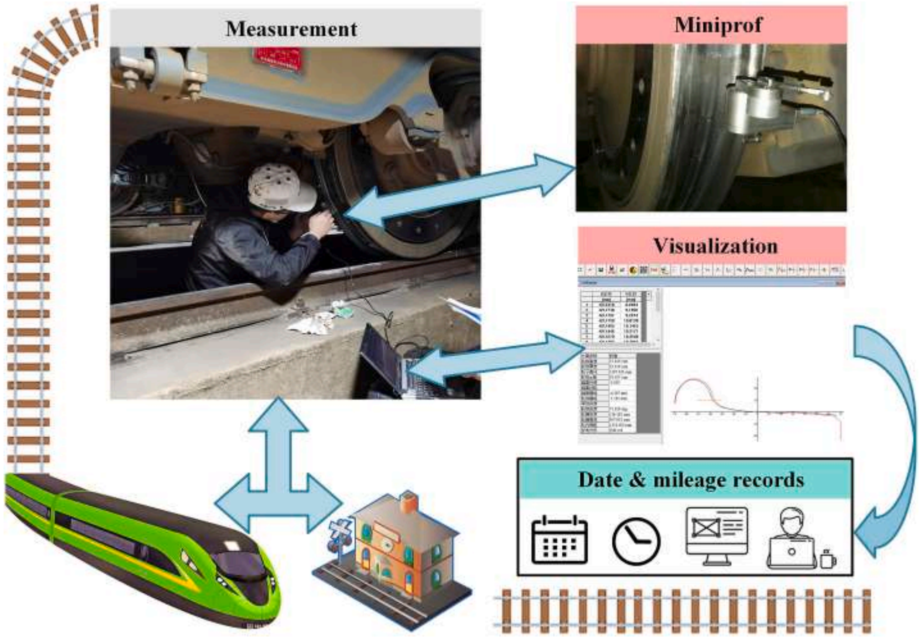

Fig. 1. Procedure for wheel wear tracking test.

Fig. 1, the monitoring protocol begins with full wheel-profile scanning using a contact-based Miniprof device, which directly measures the wheel profile with high accuracy and covers both the tread and flange regions at station depots. The collected data are immediately evaluated through a real-time visualization interface, with remeasurement carried out whenever necessary. The validated records are then indexed by accumulated operational mileage and acquisition date, providing a structured basis for subsequent wear evolution analysis.

2.2. Data processing for the wheel wear tracking test

Upon organizing the test results, it was found that there were errors in the data, which would affect the subsequent wheel-rail contact analysis and dynamic analysis. The existing errors can be divided into two types: random errors and reference point errors, as shown in Fig. 2. For random errors, Gaussian smoothing filter was first applied to the original measurement results, and then a cubic spline interpolation function was applied after sparse sampling of the data to achieve the final smoothing of the data. The adjusted results are shown in Fig. 2(a). The adjusted measurement data not only retains the overall trend of the profile but also ensures the smoothness of the data, meeting the needs of subsequent research. To address the errors in reference points, the difference between the original measurement results and the initial profile in the less frequently contacted area was used as the error evaluation function. The particle swarm optimization algorithm was employed to perform coordinate transformation on the measurement results. The results after coordinate transformation are shown in Fig. 2(b). It can be seen that the adjusted measurement results basically coincide with the initial profile.

2.3. Data statistics and analysis

A total of 376 wheel profile measurements covering different wear stages were collected. The processed measurement results are presented in Fig. 3(a and b). As the running mileage increases, both the wear width and depth exhibit a clear rising trend. The wear is predominantly concentrated around the nominal tread center, while wear near the flange is minimal, accompanied by an observable thickening of the flange. This phenomenon is attributed to the plastic flow of material induced by lateral forces.

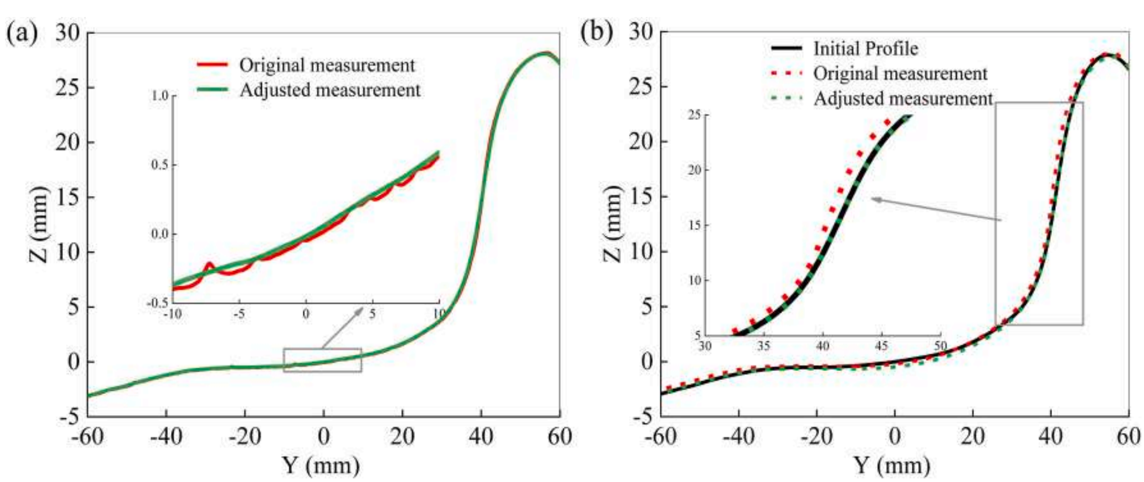

Fig. 2. Errors in measurement: (a) random errors; (b) reference point errors.

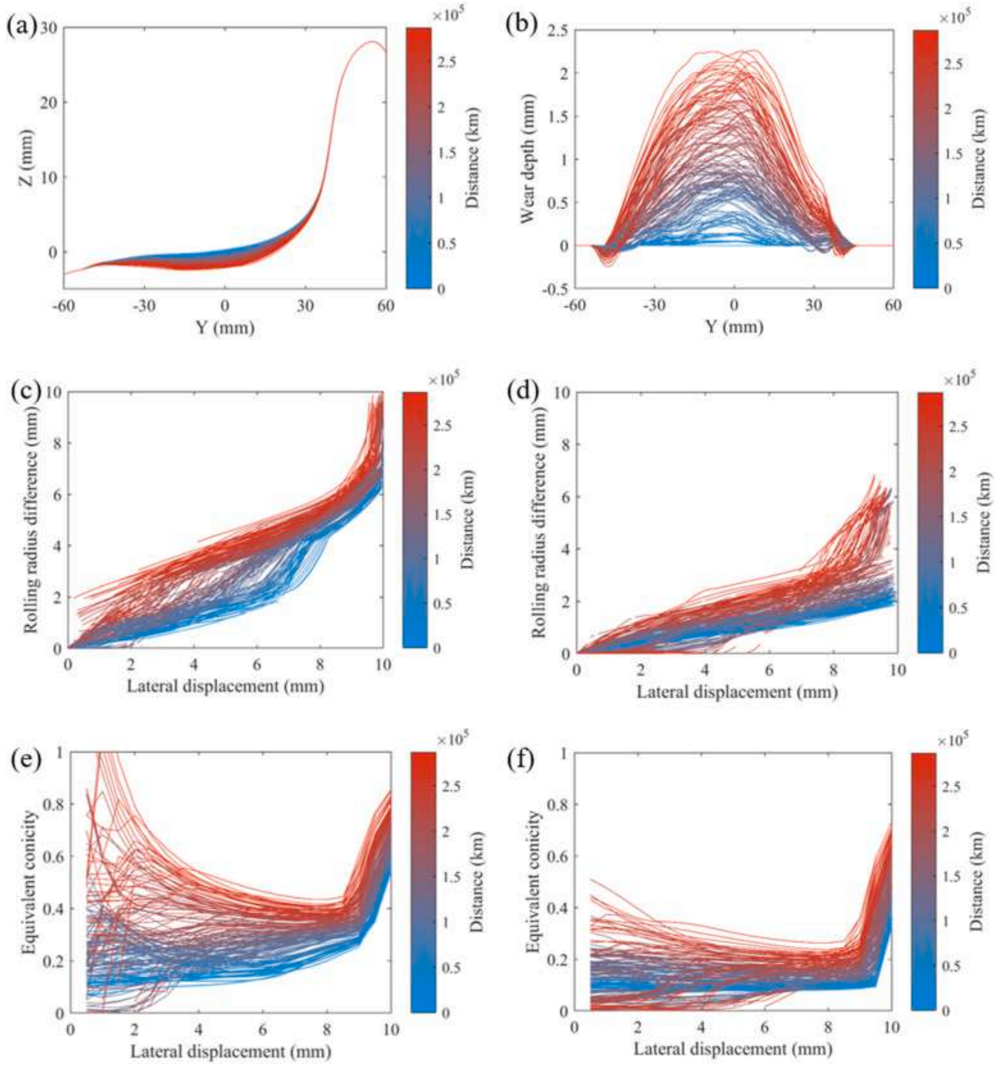

Fig. 3. Wheel wear evolution and wheel-rail contact geometry characteristics of the measured wheel profiles: (a) wheel profiles; (b) wear distributions; (c) rolling radius difference functions for the wheel profiles combined with CN60 rail; (d) rolling radius difference functions for the wheel profiles combined with CN60N rail; (e) equivalent conicities for the wheel profiles combined with CN60 rail; (f) equivalent conicities for the wheel profiles combined with CN60N rail. The calculations were performed with a rail inclination of 1:40 and a track gauge of 1435 mm.

The locomotives studied in this work mainly operate on two rail profiles: CN60 and CN60N. Compared with CN60, CN60N adopts a rail-head geometry that is more suitable for high-speed operation and generally produces lower equivalent conicity when combined with the same wheel profile. Therefore, CN60N is widely applied on Chinese railway lines adapted to high-speed transportation, since it enables a favourable wheel-rail interaction. The rolling radii difference functions $\Delta r(y)$ for the combinations of the measured wheel profiles with the two rail profiles CN60 and CN60N and the corresponding equivalent conicities were calculated using the harmonic and quasi-elastic method [34]. The default wheel-rail geometric settings adopted in the calculation, including a rail inclination of 1:40, the track gauge, the wheel back-to-back distance, and the nominal rolling-circle distance, are summarized in Table 1. The left and right wheels were treated symmetrically by using the same wheel profile in the calculation. The calculated rolling radii difference functions and equivalent conicities are shown in Fig. 3(c–f), where Fig. 3(c–e) correspond to the CN60 rail and Fig. 3(d–f) correspond to the CN60N rail. The worn wheels exhibit higher equivalent conicity when combined with the CN60 rail than with the CN60N rail, which is consistent with the higher rail-corner geometry of the CN60 profile. During the evolution of wear, the equivalent conicity changes substantially, particularly in the region of lateral displacement below 3 mm, where the dispersion of equivalent conicity becomes markedly large. Since the investigated vehicles operate on a high-speed line with large-radius curves, flange contact is unlikely and tread wear dominates; therefore, equivalent conicity is particularly sensitive to tread-profile changes. Such high dispersion indicates that even small tread-profile changes induced by wear can lead to significant variation in wheel-rail contact characteristics.

Table 1
Default wheel-rail geometric parameters used in the equivalent conicity calculation.

Parameters	value	Description
Rail inclination	1:40	Rail inclination used in the contact geometry calculation
Track gauge	1435 mm	Gauge measured at 16 mm below the rail top
wheel back-to-back distance	1353 mm	Distance between the inner wheel backs
nominal rolling-circle distance	1493 mm	Distance between the nominal rolling circles of the wheelset

The rolling radii difference function $\Delta r(y)$ reflects the changes in contact geometry more directly than the equivalent conicity, since the latter is derived from the former. Since the wear changes mostly the shape of the tread, the rolling radii difference function changes mainly in the range of low-to-moderate lateral displacements, which in turn causes a higher dispersion of the equivalent conicity for relatively low linearization amplitudes. Therefore, examining the evolution of equivalent conicity from the perspective of tread-wear morphology provides a meaningful approach for interpreting the underlying contact-geometry variation.

To further illustrate this geometric relationship, a schematic diagram is presented in Fig. 4.

As shown in Fig. 4(a), for a conical tread used here for geometric illustration, lateral displacement of the wheelset causes the left and right wheels to contact the rail at different lateral positions, thereby generating a rolling radius difference, which provides the geometric basis for the guidance and self-centering ability of the wheelset. Fig. 4(b) further illustrates three representative tread-wear morphologies, for which the worn zone, i.e., the zone in which the worn profile deviates from the original profile, is equal. POH and POL describe two cases with the same lateral position of the wear peak, i.e., the position of the maximum vertical deviation between the original and worn wheel profiles, but with different wear magnitudes. PFH represents a case with a wear magnitude similar to POH, but with the wear peak shifted laterally toward the flange side. Their corresponding equivalent conicity curves are shown in Fig. 4(c). It can be seen that, when the wear-peak position remains nearly unchanged, increasing wear magnitude mainly modifies the local profile amplitude and results in a relatively limited change in equivalent conicity. By contrast, for a similar wear magnitude, a lateral shift of the wear peak causes a much more pronounced variation in equivalent conicity. This indicates that the lateral position of the wear concentration plays a key role in the evolution of contact geometry.

Based on this observation, the nominal wear peak position is introduced to indicate the lateral location of the most worn zone on the wheel tread, and the procedure for determining it is illustrated in Fig. 5.

The actual wear peak is defined as the position of the maximum vertical deviation between the original and worn wheel profiles. A reference level is then set at 80% of this maximum wear depth, and the wear distribution curve is intersected by a horizontal line at this level. The resulting intersection interval represents the dominant worn zone, and the midpoint of this interval is defined as the nominal peak position. It should be noted that the nominal peak position only characterizes the lateral location of the dominant worn zone and does not represent the wear depth or the width of the worn zone. Moreover, the position of the actual wear peak and the nominal peak position do not necessarily coincide, as illustrated in Fig. 5.

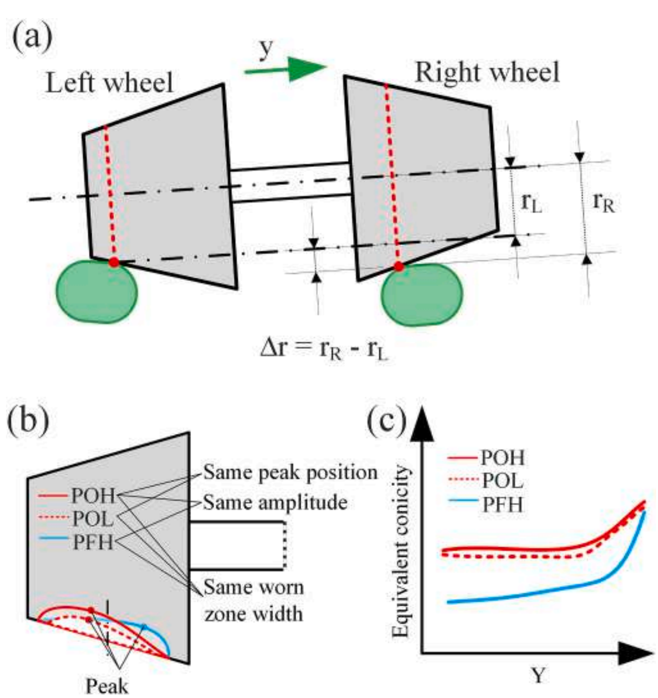

Fig. 4. Geometric interpretation of the influence of tread-wear morphology on wheel-rail contact geometry.

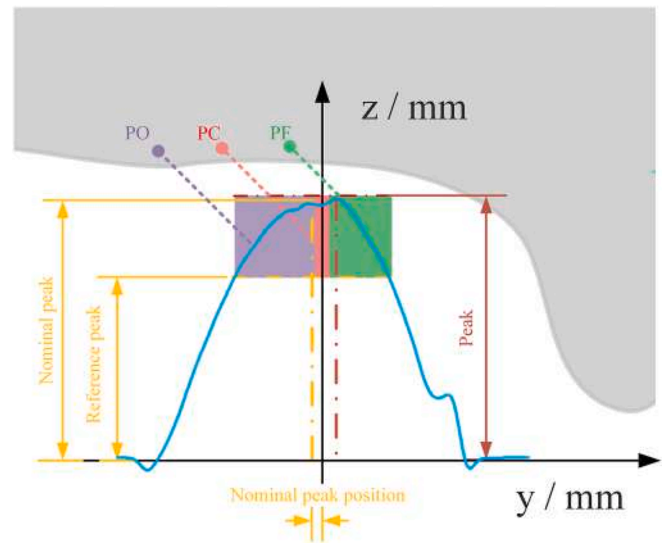

Fig. 5. Schematic diagram for determining the nominal peak position in the wear distribution.

Based on the nominal peak location, worn wheels are classified into three types.

- PC: the nominal peak lies in the interval -3 mm $\leq y \leq 3$ mm around the nominal tread center reference point.
- PF: the nominal peak lies in the range $y > 3$ mm, that is, closer to the flange side.
- PO: the nominal peak lies in the range $y < -3$ mm, that is, toward the outer side of the wheel.

The threshold of 3 mm was selected through repeated trials as the most suitable value for correlating wear distribution with equivalent conicity, although it may vary with the initial tread profile and track conditions. It should be noted that 3 mm is also a typical lateral displacement amplitude used in equivalent-conicity evaluation. This is not a purely coincidental choice, because the contact geometry in the low-to-moderate lateral displacement range is particularly sensitive to tread-wear morphology, making this range especially relevant to both classification and conicity assessment.

Using the above classification method, worn wheels with mileages over 100,000 km were combined with rail profiles, and the resulting equivalent conicity curves are shown in Fig. 6. For the CN60 rail, PF-type wheels exhibit the lowest equivalent conicity; PC-type wheels show the highest values at lateral displacement below 3 mm, whereas PO-type wheels become the highest above 3 mm. For the CN60N rail, the three wear types are clearly separated, with equivalent conicity increasing from PF to PC to PO. This confirms that nominal peak position is a useful indicator for analyzing equivalent conicity evolution under different wear distributions.

3. Vehicle dynamics and wear prediction model

The vehicle dynamic simulation model and the wheel wear prediction model have been developed and validated, providing a solid

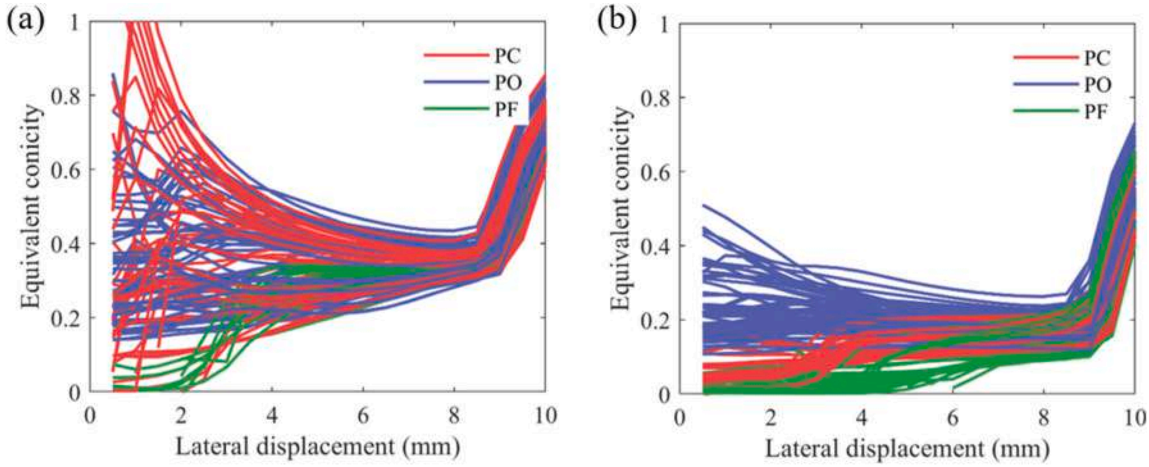

Fig. 6. Equivalent conicity distributions of different wheel wear types: (a) In combination with CN60 rail; (b) In combination with CN60N rail.

foundation for analyzing the evolution mechanism of wheel wear.

3.1. Vehicle dynamics simulation model

In power-concentrated trainsets, the traction units are concentrated on the locomotives positioned at both ends of the train, resulting in a more complex structural configuration compared with the motor cars of distributed-power EMUs. Using the dynamic parameters of the locomotives employed in the two power-concentrated trainsets, corresponding multibody dynamic models were developed in the SIMPACK multibody dynamics simulation environment.

Fig. 7(a) presents the dynamic model of the B-type locomotive. This locomotive is equipped with a two-axle bogie, has been mass-produced, and has accumulated extensive operational experience in 160 km/h power-concentrated trainsets. The nominal wheel diameter of the B-type locomotive is 1250 mm. The model features 90 degrees of freedom and is composed of 25 rigid bodies, including one carbody, two bogie frames, two traction rods, four wheelsets, four traction motors, four hollow shafts, and eight axle box arms. The primary suspension consists of axle box springs, vertical dampers, and axle box arms, while the secondary suspension comprises four lateral dampers, four yaw dampers, eight vertical dampers, four traction dampers, and eight helical coil springs. Fig. 7(b) presents the dynamic model of the C-type locomotive. This locomotive features a three-axle bogie and is currently under development for 200 km/h power-concentrated trainsets. The nominal wheel diameter of the C-type locomotive is 1050 mm. The model has 124 degrees of freedom and consists of 47 rigid bodies, including one carbody, two bogie frames, two traction rods, six wheelsets, six traction motors, six motor rotors, six gearboxes, six driving gears, six driven gears, and six gearbox suspension rods. The primary suspension is composed of axle box springs, vertical dampers, and triangular links. The secondary suspension comprises four lateral dampers, eight yaw dampers, eight vertical dampers, six motor dampers, and twelve helical coil springs.

In the multibody model, major components such as the carbody, bogie frames, wheelsets, and traction motors are represented as independent rigid bodies, whereas connecting or force-transmitting components are modelled according to their actual structural connections and principal mechanical functions, with their motions appropriately constrained where necessary. The difference in component representation between the B-type and C-type locomotives originates from their different drivetrain configurations: in the B-type locomotive, the traction motor and gearbox are integrated and are therefore represented as a single rigid body, whereas in the C-type locomotive they are modelled as separate components. To ensure computational efficiency, all vehicle components were modelled as rigid bodies, and a rigid connection was taken into account between the rail and the ground reference system. In addition, no external loads generated by external events, such as crosswind or aerodynamic interaction during train passing, were applied to the carbody in the present model. Track irregularities were introduced based on the Chinese Wu-Guang high-speed railway spectrum. Wheel-rail creep forces are computed using the FASTSIM algorithm, which offers sufficient engineering accuracy for vehicle dynamic simulations. The accuracy of the models has been validated in the previous studies [23] and [16], in which more details about the modelling of the

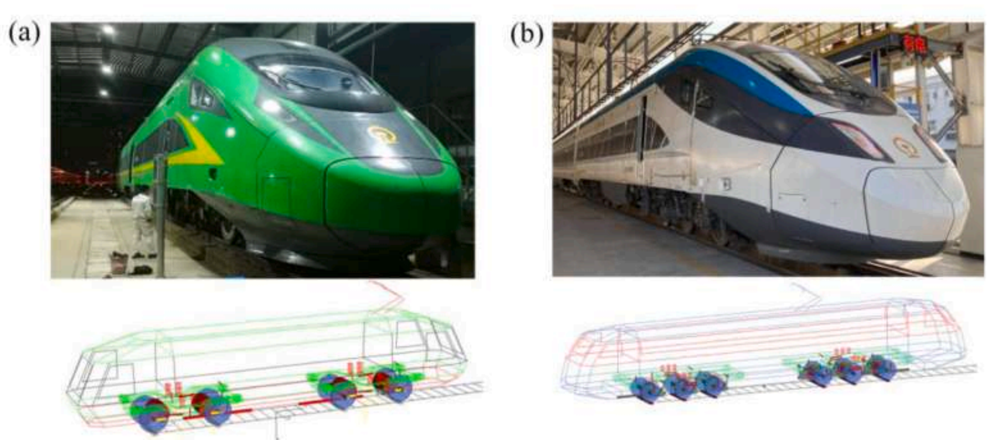

Fig. 7. Locomotive dynamic model: (a) B-type locomotive; (b) C-type locomotive.

vehicles can be found.

3.2. Wheel wear prediction model

3.2.1. General architecture

The modelling of wheel and rail wear is quite complex since it involves several fields of knowledge: vehicle dynamics, wheel-rail contact models and tribology [35]. The general architecture of the wheel wear prediction model, as depicted in Fig. 8, can be distilled into five core modules.

1) Utilizing the established locomotive dynamics model, the track composition, wheel-rail profiles, integration time, and sampling frequency are configured within the pre-processing module of SIMPACK software, thereby defining the simulation parameters.
2) Within the post-processing module of the SIMPACK software, key wheel-rail contact parameters are extracted, including the nominal tread center radius, creepages, normal force, velocities associated with creep reference points, and the dimensions of the major and minor semi-axes of the contact patch. In the wear-evaluation stage, multipoint wheel-rail contact is taken into account. Specifically, up to three simultaneous contact points are extracted in the SIMPACK post-processing and included in the wear calculation to avoid missing contact contributions under multi-contact conditions. These contact quantities are obtained under the Hertzian contact assumption and are used as the baseline contact inputs for the subsequent wear calculation.
3) The wheel-rail contact parameters are integrated into the contact model, with the Hertzian theory utilized to calculate the distribution of normal stresses across the contact patch. Subsequently, the FASTSIM algorithm is applied to determine the tangential stresses within the contact patch.
4) In the wear model, the wear contribution associated with each contact point is calculated and mapped onto the wheel profile. For multipoint contact cases, the wear contributions from individual Hertzian contact points are evaluated separately and then superposed according to their lateral contact positions. When the local contact state satisfies the predefined non-elliptic contact criterion, a local non-Hertzian correction is introduced. This correction does not replace the Hertzian contact results extracted from SIMPACK; instead, it redistributes the predicted material removal within the contact patch while keeping the total material removal unchanged. Furthermore, considering the sampling frequency, nominal tread center radius, creep reference velocity, and actual simulated distance, the wear weighting value specific to a single contact point is derived. The resulting wear is then extrapolated to a 5000 km update interval according to the ratio between the simulated distance and 5000 km. Under this interval, the wheel wear depth in each iteration generally remains below 0.1 mm, which is acceptable for iterative wear simulation.
5) Under the symmetric-wear assumption, the wear-depth distributions of the left and right wheels within the same wheelset are mirrored, averaged, and smoothed. The resulting material removal distribution is then overlaid onto the wheel profile, which serves as the basis for the subsequent computational iteration. This iterative process is continuously cycled to accomplish the prediction of wheel wear progression, aligned with the accumulated mileage of the locomotive.

From a methodological perspective, the present study adopts a relatively simple and conventional wheel–rail contact model based on Hertzian normal contact and the original FASTSIM algorithm. It is recognized that more advanced non-Hertzian contact models and wear formulations have been developed in recent decades [36] [37], and that the Hertz-FASTSIM framework, although efficient and widely used in vehicle dynamic simulations, has limitations in local wear evaluation. In the present study, a fully non-Hertzian contact formulation was not adopted as the primary solver for the time-domain vehicle dynamics

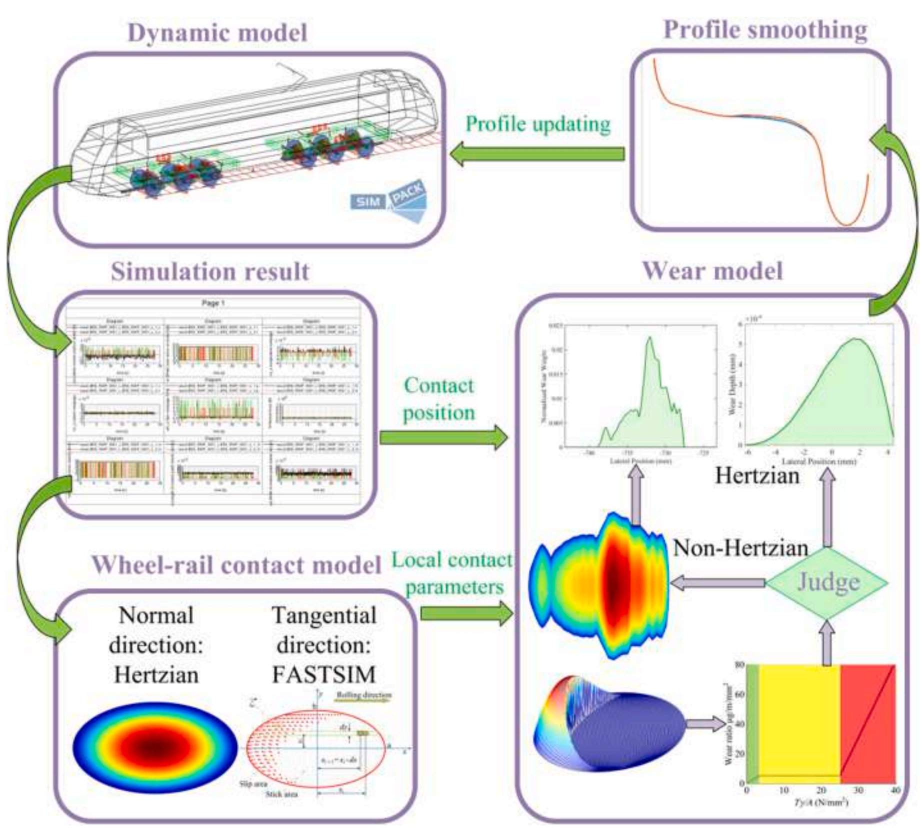

Fig. 8. General architecture of the wear prediction model.

integration, because the repeated wear simulations require a computationally efficient and numerically robust framework. To account for these non-Hertzian effects without sacrificing efficiency, a local non-Hertzian correction was introduced in the wear-evaluation step. The Hertz-FASTSIM solution is retained for the global dynamic simulation, while the local wear redistribution is corrected when the contact state satisfies the predefined non-Hertzian criterion. Moreover, the high-speed locomotives investigated here predominantly operate on large-radius curves, for which wheel–rail contact mainly occurs in the tread region. Under these operating conditions, the Hertz-FASTSIM framework remains suitable as the system-level contact solver for long-term wear prediction, while the local non-Hertzian correction improves the physical fidelity of wear redistribution when non-Hertzian contact conditions arise. For more severe cases involving pronounced conformal contact, flange-dominated contact, or substantial plastic deformation, more advanced non-Hertzian or elastoplastic formulations would be required. Therefore, the proposed framework provides a practical balance between computational cost, numerical robustness, and modelling accuracy.

3.2.2. Wheel-rail contact model

The construction of the wheel-rail contact model is pivotal in the wear prediction model, primarily dedicated to determining the distribution of normal and tangential forces across the contact patch, which in turn ascertains the local creep rates within the slip region. The Hertzian contact theory and the FASTSIM algorithm, recognized for their extensive application in addressing wheel-rail contact force issues, have been selected for use in this study. The FASTSIM algorithm discretizes the contact patch into strips along the rolling direction and evaluates the local stick and slip conditions. Fig. 9 illustrates the resulting concept of local creep rate distribution within the contact patch.

The FASTSIM algorithm is employed to calculate the distribution of tangential stresses within the contact patch, as demonstrated in Eq. (1).

$$\begin{cases} \tau_x(x_{i+1}, y_i) = \tau_x(x_i, y_i) - \left(\dfrac{v_x}{L_x} - \dfrac{\phi y_i}{L_\phi}\right) dx \\ \tau_y(x_{i+1}, y_i) = \tau_y(x_i, y_i) - \left(\dfrac{v_y}{L_y} - \dfrac{\phi x_i}{L_\phi}\right) dx \end{cases} \tag{1}$$

where τ_x and τ_y represent the tangential stresses in the longitudinal and lateral directions, respectively. dx denotes the longitudinal grid spacing, v_x is the longitudinal creep rate, v_y is the lateral creep rate, and ϕ is the spin creep rate. L_x, L_y, and L_ϕ represent the longitudinal, lateral, and spin flexibility coefficients, respectively, all of which are defined according to the FASTSIM algorithm [38].

The present Hertz–FASTSIM framework is retained as the primary contact solver for the system-level wear simulation, while a local non-Hertzian correction adopted in the wear-evaluation step is described separately in Section 3.2.4.

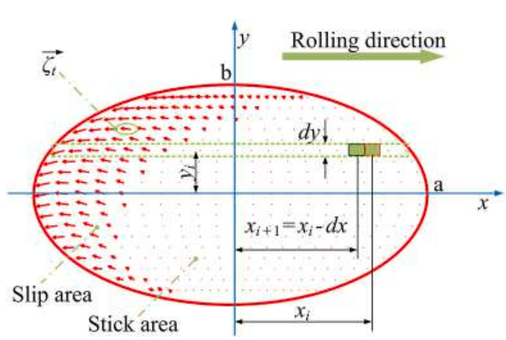

Fig. 9. Distribution of local creep rate in contact patch.

3.2.3. Wear model

Lewis analyzed wear data for various wheel–rail material combinations and established a wear-rate function in terms of the wear index [39]. This function is divided into three distinct regimes: mild wear, severe wear, and catastrophic wear [40]. In the present study, the wear-rate function calibrated for U71Mn steel was adopted. For consistency with the adopted wear-rate function, both contacting bodies were represented by U71Mn steel in the wear calculation as a simplifying assumption. The chemical composition and microstructure of this material follow the descriptions in Ref. [41]. The wear-rate function was obtained from twin-disc tests conducted using the apparatus shown in Fig. 10 [43] [42]. The wear-rate function is analytically expressed as follows:

$$K_w = \begin{cases} 3.58T\gamma/A & T\gamma/A < 5 \\ 17.9 & 5 \le T\gamma/A \le 20 \\ 12.3T\gamma/A - 228 & 20 < T\gamma/A \end{cases} \tag{2}$$

where K_w (unit:μg/(m·mm^2) is the mass of material removed per unit rolling distance and per unit contact area within the contact patch. The quantity $T\gamma/A$ (unit: N/mm^2) is adopted as the wear index averaged over the nominal contact area, hereafter referred to as the area-averaged wear index, where T, γ, and A denote the tangential force, creepage, and nominal contact area [44], respectively. Following Ref. [44], it represents the work done per unit nominal contact area and per unit rolling distance. The three regions in Eq. (2) correspond to mild wear for $T\gamma/A < 5$ N/mm^2, severe wear for $5 \le T\gamma/A \le 20$ N/mm^2, and catastrophic wear for $T\gamma/A > 20$ N/mm^2.

Within the contact patch, the wear depth h (unit:μm) is calculated by:

$$h(x_i, y_i) = \frac{K_w}{\rho} dx \tag{3}$$

where ρ represents the material density, taken as 7800 μg/mm^3.

3.2.4. Local non-Hertzian correction for wear redistribution

In the present correction, the wheel is treated as a body of revolution and the rail as an extruded body along the longitudinal direction. Therefore, the local wheel-rail geometric relation can be analyzed in the transverse profile plane. The gap function $g(y)$ denotes the undeformed normal gap between the wheel envelope and the rail profile along the lateral coordinate y [45].

A dual geometric criterion is introduced to identify non-Hertzian contact states. At each simulation step, the gap function $g(y)$ is examined from two aspects. First, the local minima of $g(y)$ are identified. If more than one distinct minimum exists within the potential contact

Fig. 10. Twin-disc test apparatus [42].

zone, the non-Hertzian correction is activated. Second, the gap profile $g(y)$ is fitted by a quadratic polynomial $g_{\mathrm{fit}}(y)$ using the least-squares method, and the parabolic deviation index is defined as

$$E_{\mathrm{dev}} = \frac{\max \left| g(y) - g_{\mathrm{fit}}(y) \right|}{\delta} \tag{4}$$

where δ is the normal approach, which is determined by imposing the normal load equilibrium over the entire contact region. When E_{dev} exceeds a prescribed tolerance threshold (10%), the non-Hertzian correction is also activated. Once activated, the local normal compression is written as

$$c(y) = \max\,(0, \delta - g(y)) \tag{5}$$

Based on a strip-based semi-Hertzian approximation [36,46–48], the longitudinal semi-length of each strip is

$$a(y) = \sqrt{2R_0\, c(y)} \tag{6}$$

where R_0 is the nominal rolling radius. Following the assumption of a semi-elliptic normal pressure distribution along the rolling direction, the normal-load density associated with each strip is then approximated by

$$F_{\mathrm{strip}}(y) = \frac{\pi}{4} E^{*}\, c(y) \sqrt{2R_0\, c(y)} \tag{7}$$

where E^{*} is the equivalent elastic modulus. Accordingly, the weighting factor used for wear redistribution is defined as

$$\omega(y) = \frac{F_{\mathrm{strip}}(y)}{\int F_{\mathrm{strip}}(y)\, \mathrm{d}y} \tag{8}$$

The total material removal predicted by the original Hertz-FASTSIM-based wear calculation is then redistributed among the strips according to $\omega(y)$, while keeping the total wear amount unchanged. The tangential force, creepage, and total material removal are still obtained from the Hertz-FASTSIM-based wear model, and the local non-Hertzian correction is only used to modify the lateral distribution of material removal within the contact patch. In this way, the proposed treatment preserves computational efficiency while improving the physical fidelity of local wear redistribution under non-Hertzian contact conditions.

3.2.5. *Model validation*

Simulation conditions were established based on the operating conditions of the reference locomotives on the Chang-bai High-Speed Railway, whose aerial view is shown in Fig. 11(a). The simulation conditions include the rail profiles, the percentage of straight and curved track, curve curvature, curve superelevation, operating speed, axle torque, rail inclination, and friction coefficient. Among them, the rail profiles include both standard rail profiles and the rail profiles measured using a Miniprof device, as shown in Fig. 11(b). The standard rail profiles consist of the CN60 and CN60N rails. Two profiles selected from the measured rails were used to represent a normally worn rail (CN60M) and an extremely worn rail (CN60EP), respectively, as shown in Fig. 11 (c). Although the exact along-line distribution of the rail profiles was not available, internal maintenance records indicated that CN60 and CN60N were used in mixed service on the investigated railway. In addition, the measured worn profiles CN60M and CN60EP both originated from CN60 rail in straight-line sections and were therefore introduced in the validation stage to represent typical worn rail conditions observed in service. These four rail profiles were combined in a certain percentage and

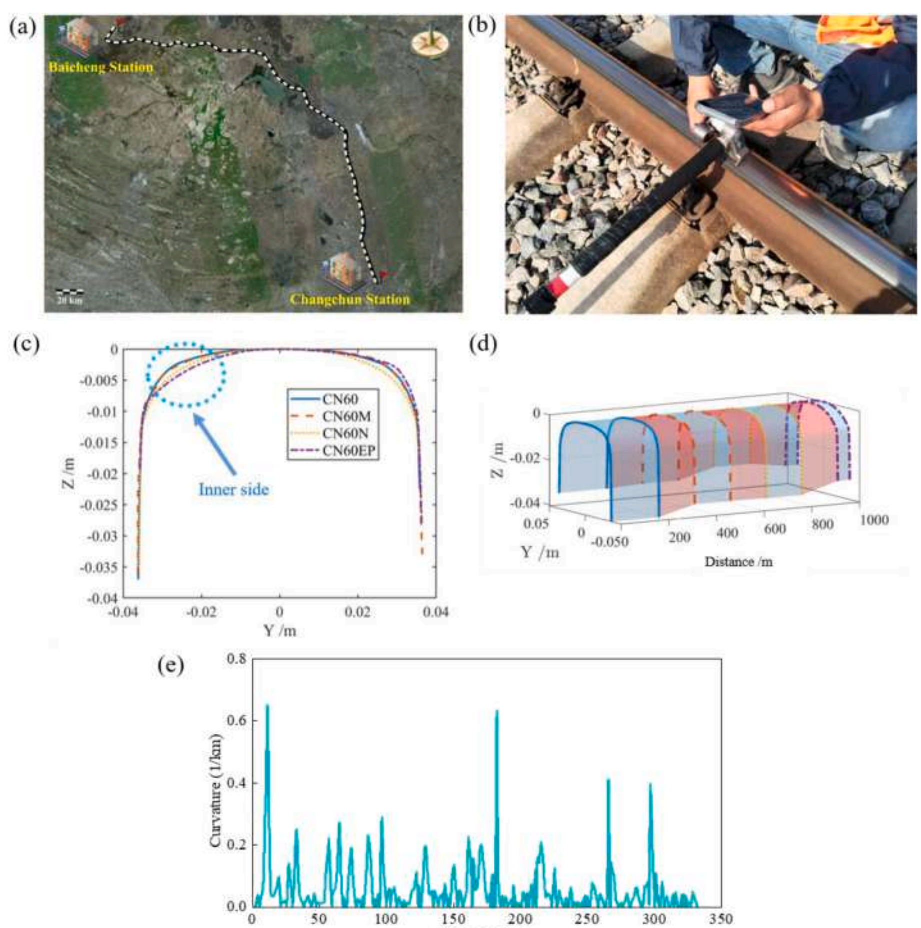

Fig. 11. Chang-bai High-Speed Railway: (a) Railroad map; (b) Rail profile measurement; (c) Rail profile; (d) Rail profile composition; (e) Track layout.

with linear transitions to form a typical track, as illustrated in Fig. 11(d).

It should be noted that the rail-profile setting used in the validation stage differs from that used in the subsequent parametric wear analysis. For model validation, standard and worn rail profiles were combined to reproduce representative measured line conditions, whereas in the later analysis only the two standard rail profiles, CN60 and CN60N, were considered in combination to provide a more general basis for comparing the influence of rail-profile conditions. The curvature distribution of the Chang-bai High-Speed Railway is presented in Fig. 11 (e). Sections with radii exceeding 20,000 m were treated as straight track, giving a straight-line percentage of 79.8%. The distribution of curved segments, together with their corresponding superelevation settings and default running speeds, is summarized in Table 2. These parameters serve as representative operational scenarios for the iterative wear simulation. The friction coefficient was taken as 0.3, which is a commonly adopted engineering value in long-term vehicle dynamic and wear simulations and is also consistent with previous simulation and test experience of the research team. Track irregularities were introduced according to the spectrum described in Section 3.1 and were kept unchanged in the validation simulations.

The dynamic simulation was conducted on simplified representative short straight and curved track segments rather than on a full reconstruction of the measured line. For the curved-track conditions, each curve-radius class listed in Table 2 was represented by one corresponding simulation scenario. The rail profiles used for the curved-track simulations were representative rail profiles measured from the curved sections of the investigated line, rather than profiles randomly assigned to different curve-radius classes. The wear generated under straight- and curve-track conditions was calculated separately and then extrapolated to long-term mileage through a weighted scaling procedure according to the prescribed proportions of straight and curved sections, curve-radius classes, and rail profiles.

These simulation conditions also serve as the parameters for subsequent analyses, and their specific values are provided in Section 4.1. To validate the accuracy of the proposed wear prediction model, the simulation results were compared with field measurements. Eight successive measurements of the wheel profile of a high-speed locomotive operating on the Chang-bai High-Speed Railway were collected within a single re-profiling interval. During the wear prediction simulation, the wheel profile was periodically updated at intervals of 5000 km. To facilitate comparison with the measurements and improve interpretability, the simulated wear depth was projected along the normal direction onto the original tread profile, and the vertical wear distribution was obtained by subtracting the original profile from the worn one. Moreover, because the operating mileage associated with the field measurements was not recorded as exact integers, the measured profiles were adjusted to the nearest corresponding mileage ratios. Taking the leading wheelset as an example, profiles corresponding to approximately 50,000 km, 100,000 km, and 150,000 km were selected for comparison. Unless otherwise stated, all subsequent analyses are based on the leading wheelset of the leading bogie, since it experiences the most severe tread wear in the present vehicle configuration.

Table 2
Geometric parameters and operational settings for curved segments.

Radius	Ratio	Superelevation	Default running speed
1600 m	0.23%	70 mm	100 km/h
2000 m	0.46%	50 mm	110 km/h
2800 m	0.98%	40 mm	120 km/h
3500 m	0.91%	40 mm	130 km/h
5000 m	3.72%	40 mm	140 km/h
8000 m	8.31%	20 mm	150 km/h
20000 m	5.59%	10 mm	160 km/h

Note. The curve parameters and operational speeds listed in this table are simplified representative values used for numerical wear simulation. These values are approximate and intended for characteristic analysis; they may deviate from the actual field conditions of the Chang-bai High-Speed Railway.

Fig. 12 compares the simulated wheel-wear distribution with the measured results obtained using the Miniprof device. As described in Section 2.1, the measured results shown in Fig. 12 were gained for the wheels of Type B locomotives. The wear development of the B-type locomotive is notably slower than that of the C-type locomotive, which is mainly attributed to the larger nominal wheel diameter of the B-type locomotive (1250 mm) compared with that of the C-type locomotive (1050 mm). As a result, the smaller-diameter wheels of the C-type locomotive experience more contact cycles per unit mileage and therefore accumulate wear more rapidly. In addition, the simulated wear-affected zone on the wheel tread is narrower than the measured one because the present model does not consider external loads generated by external events, such as crosswind, vortex-induced vibration in single-track tunnels, turnout negotiation, and train passing events. Overall, the good agreement between the simulation and measurement results confirms the effectiveness of the wear prediction model developed in this study.

4. Factors and mechanisms of wheel wear evolution

Building on the measured data and the validated simulation framework, this section identifies the dominant factors affecting wheel wear. The analysis is structured into three categories: driving requirements, track conditions, and locomotive type. For each category, the associated mechanisms and their effects on wheel–rail contact conditions and wear evolution are systematically examined.

4.1. Design of parameter combinations

Wheel wear prediction involves the simultaneous execution of the vehicle dynamics model, the wheel-rail contact model, and the material wear model. As a result, the computational cost is high. Therefore, rather than reconstructing the full measured line directly in the multibody simulation, a one-factor-at-a-time parametric sensitivity analysis was carried out based on simplified representative operating and track conditions. In this framework, straight-track and curve-track conditions were simulated separately on representative short segments, and the corresponding wear results were combined through a weighted scaling procedure according to the prescribed proportions of straight and curved sections to estimate long-term wear evolution. Thus, the objective of this section is not to reproduce the exact spatial sequence of the measured line, but to evaluate the relative influence of representative track and operating factors on wear evolution. Based on the research team's experience in wheel–rail wear studies and the typical operating conditions adopted in previous modelling work, seven influencing factors were selected as variables for the wear analysis.

- P1: Percentage of rail profiles (various combinations of CN60 and CN60N)
- P2: Curve mileage ratio
- P3: Superelevation scaling factor for the representative curves
- P4: Operating-speed scaling factor for straight-track simulations
- P5: Axle-torque scaling factor for straight-track simulations
- P6: Rail inclination
- P7: Wheel–rail friction coefficient

Here, P1 denotes the mileage percentage of the two representative rail profiles, CN60 and CN60N, in the simplified track condition, with their sum equal to 1. Although four measured rail profiles were considered in constructing the representative track in Section 3.2.4, only the two representative profiles CN60 and CN60N were retained as independent variables in the present sensitivity analysis in order to keep the parameter combinations tractable. P2 denotes the mileage percentage of curved sections in the representative track condition, where 0 corresponds to a pure straight-track condition, and 0.2 and 0.4

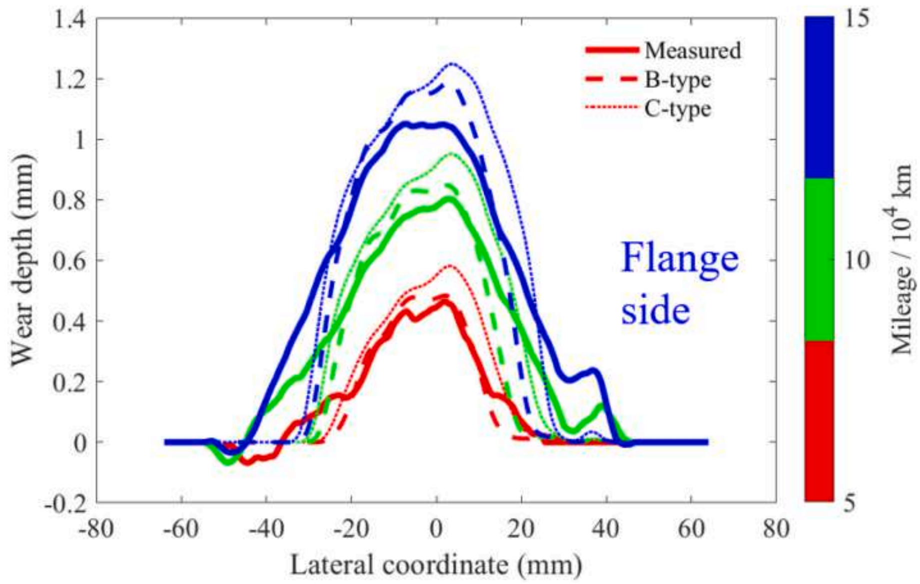

Fig. 12. Comparison of wear measurement and simulation results.

indicate that curved sections account for 20% and 40% of the representative mileage, respectively. P3 denotes a uniform scaling factor applied to the baseline superelevation values listed in Table 2. P4 and P5 are applied only in the straight-track simulations; in the curve-track simulations, the running speed is fixed according to Table 2 and no driving torque is applied.

Based on the wheelset rotational torque conditions observed during actual locomotive operation, the longitudinal loading conditions were

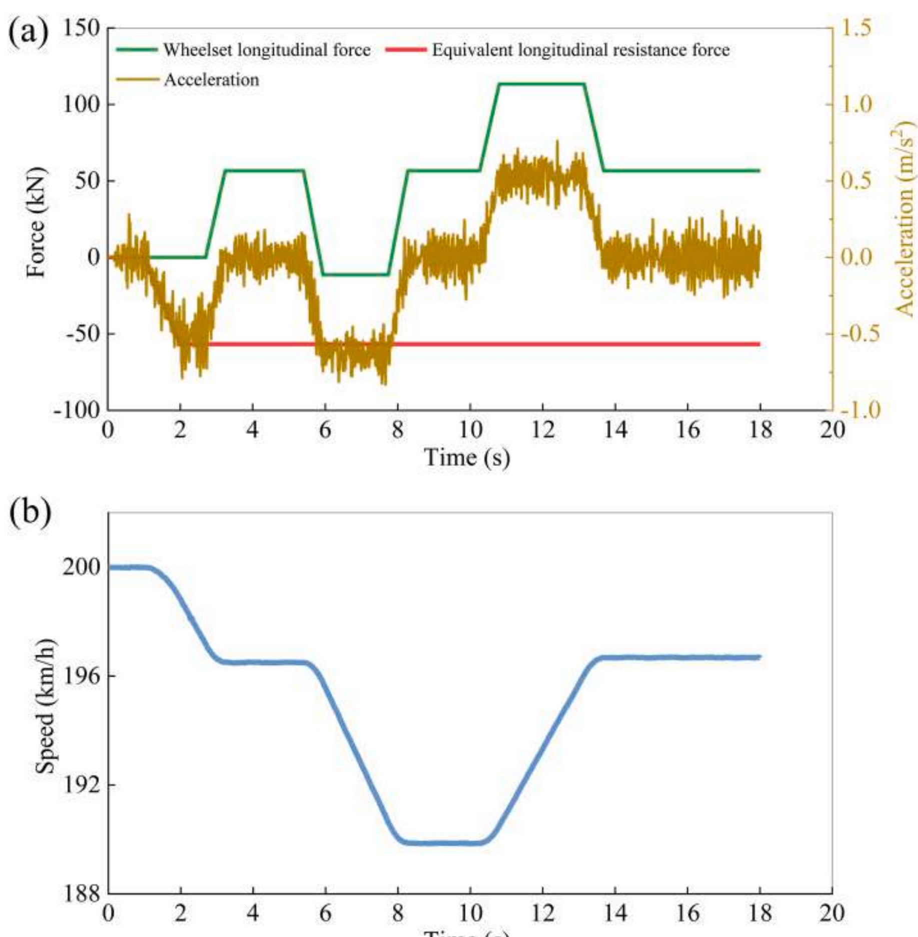

Fig. 13. (a) Prescribed time histories of wheelset longitudinal force, equivalent longitudinal resistance force, and the corresponding longitudinal operating acceleration; (b) corresponding running-speed history for the representative 200 km/h case.

defined accordingly. For the straight-track simulations of the C-type locomotive, seven initial speeds ranging from 80 to 200 km/h at intervals of 20 km/h were considered, with identical proportions assigned to each speed condition. The initial speeds for the B-type locomotive were proportionally scaled by a factor of 0.8 relative to the C-type locomotive to account for the difference in their maximum operational speeds.

Fig. 13 shows the prescribed time histories of wheelset longitudinal force and equivalent longitudinal resistance force used in the straight-track simulations of the C-type locomotive, together with the corresponding running-speed history for the representative case with an initial speed of 200 km/h. Here, the equivalent longitudinal resistance force is an empirical loading curve used to represent the combined longitudinal resistance acting on the locomotive during operation, including the running resistance and the longitudinal resistance transmitted from the hauled trainset. It is not intended to separately calculate each individual resistance component, but to provide a representative longitudinal loading condition for the simulation. At the beginning of the simulation, this force is gradually increased from zero to its prescribed value to avoid a sudden load application and to ensure a smooth introduction of the longitudinal load into the SIMPACK model. In this case, the simulation duration is 18 s, corresponding to a representative simulation distance of 1000 m. For other initial-speed conditions, the same loading pattern is retained, while the total simulation time is adjusted proportionally to maintain the same simulation distance. The corresponding longitudinal operating acceleration is derived from the simulation. In evaluating the effect of axle torque on wheel wear, the torque level is uniformly scaled using proportional amplification or reduction, while the prescribed initial speed level is kept unchanged. Although the running speed is dynamically coupled with the applied torque, the additional speed variation induced by the torque scaling remains limited. For the representative 200 km/h case, the overall torque-scale range considered in Table 3 leads to only about a 1% variation in the resulting speed history, which is sufficiently small for the present controlled-comparison analysis. To ensure consistency in the comparative analysis, the operating acceleration range of the B-type locomotive is constrained to that of the C-type locomotive.

Table 3 summarizes the default parameter set P0, along with two alternative values for each of the seven influencing factors. By varying one factor at a time while keeping the remaining six parameters at their default values, 14 single-factor perturbation combinations (P11–P72) were constructed. Together with P0, a total of 15 parameter combinations were generated. These combinations form the basis for evaluating the effects of each influencing factor on the nominal wear peak position and its evolution with increasing service mileage.

To improve computational efficiency and to identify the dominant influencing factors, the simulation analyses were limited to the first 50,000 km of wheel wear. For convenience, the seven influencing factors are referred to as P1–P7 in the following discussion.

4.2. Identification of dominant influencing factors

Fifteen parameter combinations were evaluated for both the B-type and C-type locomotives. After 50,000 km of simulated service, the resulting tread wear was quantified by the nominal peak position and wear depth, as shown in Fig. 14(a and b) for the B-type locomotive and Fig. 14(c and d) for the C-type locomotive. In the following analysis, the lateral coordinate is consistent with the definition in Fig. 5: 0 mm denotes the nominal rolling circle, and positive values indicate the flange side.

From Fig. 14(a–c), it can be observed that the nominal peak position of the B-type wheel profile is located farther toward the tread exterior compared with that of the C-type wheel. This difference is associated with the axle arrangements of the two locomotive types. For the mechanism analysis, an additional set of straight-track dynamic simulations was carried out separately for the two locomotive types. To facilitate a clearer comparison of the contact-point distribution between the two vehicle types, the simulation distance in this analysis was extended to 2500 m for presentation only. Here, the contact position denotes the lateral coordinate of the dominant wheel-rail contact point extracted from the Hertzian contact results. For cases with multipoint contact, the contact point with the largest normal force was used for the comparison. The time histories of contact position along the running distance were then extracted for the B-type locomotive at a prescribed initial speed of 160 km/h and for the C-type locomotive at prescribed initial speeds of 160 km/h and 200 km/h. The resulting contact-point distributions are shown in Fig. 15.

As can be seen from Fig. 15, the contact points of the B-type locomotive are distributed farther away from the flange, whereas those of the C-type locomotive are located closer to the flange side. This tendency can be recognized from the higher positive peaks of the C-type locomotive, especially for the 200 km/h case. Since positive contact-position values correspond to locations closer to the flange, the C-type locomotive is more prone to accumulate material removal in the region close to the flange. This is also consistent with the nominal peak positions shown in Fig. 14(a–c). In the flange-side region, the larger local profile inclination increases the spin creepage component, which may intensify material removal compared with the central tread region. Fig. 14(a–c) also shows that several factors have a notable effect on the location of the nominal wear peak position. Increasing the percentage of CN60 rail profiles, reducing rail inclination, increasing running speed, and decreasing axle torque all contribute to shifting the nominal peak

Table 3
Parameter combinations for the seven influencing factors (P0 and P11–P72).

Name	Percentage of rail profiles		Curve mileage ratio	Superelevation scaling factor	Speed scaling factor	Axle-torque scaling factor	Rail inclination (1:n)	Wheel-rail friction coefficient
	CN60	CN60N						
P0	0.2	0.8	0.2	1	1	1	1:40	0.3
P11	0.6	0.4	0.2	1	1	1	1:40	0.3
P12	0.8	0.2	0.2	1	1	1	1:40	0.3
P21	0.2	0.8	0	1	1	1	1:40	0.3
P22	0.2	0.8	0.4	1	1	1	1:40	0.3
P31	0.2	0.8	0.2	0.8	1	1	1:40	0.3
P32	0.2	0.8	0.2	1.2	1	1	1:40	0.3
P41	0.2	0.8	0.2	1	0.8	1	1:40	0.3
P42	0.2	0.8	0.2	1	1.2	1	1:40	0.3
P51	0.2	0.8	0.2	1	1	0.9	1:40	0.3
P52	0.2	0.8	0.2	1	1	1.1	1:40	0.3
P61	0.2	0.8	0.2	1	1	1	1:35	0.3
P62	0.2	0.8	0.2	1	1	1	1:45	0.3
P71	0.2	0.8	0.2	1	1	1	1:40	0.24
P72	0.2	0.8	0.2	1	1	1	1:40	0.36

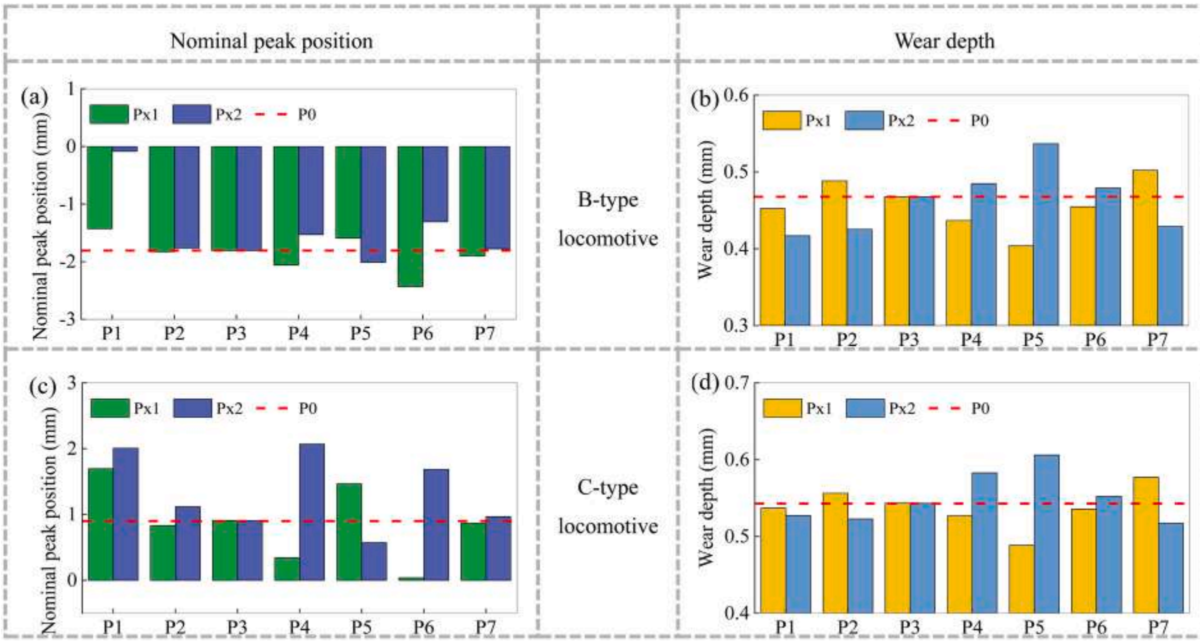

Fig. 14. The influence of different factors on the wheel wear.

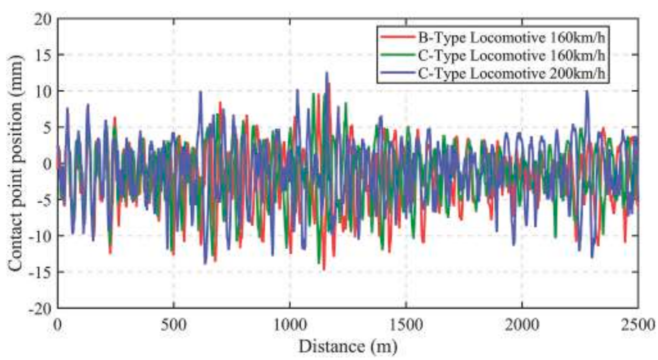

Fig. 15. Wheel–rail contact comparison for B-type and C-type locomotives: contact-position distributions along the running distance for additional straight-track mechanism-analysis cases.

position toward the wheel flange.

From Fig. 14(b–d), it can be seen that the wear progression of the B-type wheel is slower than that of the C-type wheel, mainly because the wheel diameter of the B-type locomotive is larger. Moreover, increasing the proportion of CN60 rails, increasing the percentage of curves, increasing rail inclination, increasing the wheel–rail friction coefficient, and reducing running speed and axle torque all reduce the wear depth. Overall, rail profile, rail inclination, running speed, and axle torque exhibit the most significant effects on wear behaviour, indicating that these four factors merit further detailed analysis.

4.3. Mechanistic analysis of the dominant factors

The effects of rail profile and rail inclination on wheel wear can be interpreted from the perspective of wheel–rail contact geometry. Considering quasi-elastic corrections, the wheel-rail contact line method was applied to determine the distribution of wheel–rail contact points for different rail profiles and different values for the rail inclination [45]. The line method considers the wheelset as a rigid body and the running surface as a surface of revolution. By projecting the wheel surface on a normal plane to the rail the three-dimensional problem, which deals with surfaces, can be reduced to a two-dimensional one considering curves, which simplifies the analysis. In this analysis, the economically re-profiled JM3 tread (defined in Section 2.1) is explicitly used as the reference wheel profile to maintain consistency with the field tracking test.

The results are shown in Fig. 16, where color gradients are used to represent different values of the relative lateral displacement of the wheel, and the nominal tread center reference position is marked with an arrow for clarity. As illustrated in Fig. 16(a), (c), and 16(e), which show the results obtained for the CN60 rail profile, the contact points are distributed in a relatively continuous and homogeneous way across the running surfaces of the wheel and rail. In contrast, the results displayed in Fig. 16(b), (d), and 16(f), which are obtained for the CN60N rail profile, show a more strongly discontinuous distribution. In these cases, for most lateral displacements, the wheel-rail contact occurs in a relatively narrow zone located around the tread centers of both the wheel and rail. However, when the lateral wheel displacement to the left exceeds 10 mm, the contact points jump to the wheel flange and the rail corner. The fact that, for the CN60N rail profile, the contact points remain in the narrow central zone of the wheel tread for most displacements indicates a relatively small variation in rolling radius, which explains the low equivalent conicity obtained for this rail profile. Furthermore, the distribution of the contact points indicates that wear tends to be concentrated in the central zone of the wheel tread, while the region between the central zone and the wheel flange is practically unaffected by wear, since no contact occurs in this region.

As the percentage of CN60 rails increases, the load distribution near the central tread decreases, resulting in a reduction in wear depth and a shift of the nominal wear peak toward the flange. This is because the wider contact distribution of the CN60 rail avoids the excessive concentration of tangential contact forces within a narrow band, thereby mitigating the rapid progression of localized wear. The contact points move toward the flange and the contact band becomes narrower for a lower rail inclination. This concentrates the load near the flange, leading to deeper wear and shifting the nominal peak toward the flange.

Running speed and acceleration are two key controllable parameters related to driver operating requirements, and their influence on wheel wear is associated with vehicle dynamic behaviour. The operating acceleration is primarily affected by the axle torque. Using the C-type locomotive as an example, Fig. 17(a and b) presents the statistical distributions of wheel–rail contact point locations under different running

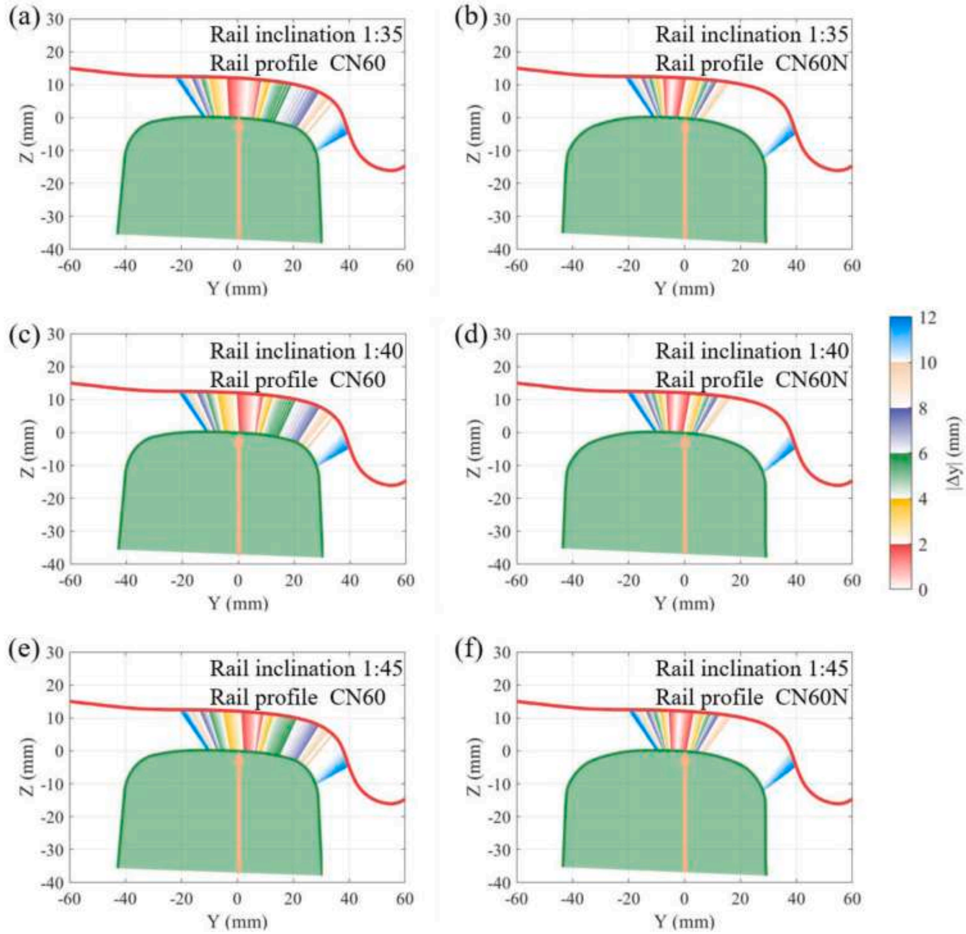

Fig. 16. Wheel–rail contact point distribution under different rail profiles and rail inclinations, calculated using the economically re-profiled JM3 tread as the reference wheel profile.

speeds and axle torques. Fig. 17(a) shows boxplots of the contact point position, where the lower and upper bounds of the box represent the first and third quartiles, and the line inside the box indicates the median. The blue circles denote outliers, namely samples beyond the typical range of the distribution. As a complement, Fig. 17(b) shows the probability density functions of the contact point position. The horizontal axis denotes the contact position and the vertical axis denotes the probability density, with each curve representing the distribution for one parameter case. Fig. 17(a and b) indicates that higher running speed shifts the contact points toward the flange, whereas axle torque has only a minor influence on the contact point location.

To further quantify how wear is distributed along the tread, the contact band was divided into windows with a step of 0.5 mm, and the mean wear number within each window was calculated. It should be noted that the wear number $T\gamma$ represents the energy dissipated in the contact per unit rolling distance, whereas $T\gamma/A$ denotes the area-averaged wear index introduced in Section 3.2.3. The speed-related results are shown in Fig. 17(c), and the axle-torque-related results are shown in Fig. 17(d). Fig. 17(c and d) shows that increasing speed increases the wear level near the flange, while higher axle torque increases the wear number closer to the nominal tread center. Therefore, increasing running speed and reducing axle torque both contribute to shifting the nominal wear peak toward the flange.

4.4. Evolution of wheel wear and wheel–rail contact geometry

4.4.1. Comparison of locomotives under default parameters

Under the default parameter set P0, long-distance wear simulations of 180,000 km were performed for both the B-type and C-type locomotives to investigate the evolution of wear types with increasing mileage. Fig. 18(a and b) presents the tread wear distributions for both locomotive types across the full mileage range; the horizontal axis denotes lateral tread position and the vertical axis denotes wear depth, while different colors indicate different service mileages.

As shown in Fig. 18, the nominal wear peak of the B-type locomotive wheel is initially located near the nominal tread center. As wear progresses, the peak gradually migrates toward the tread exterior so that eventually a characteristic PO-type wear pattern develops. By contrast, the C-type locomotive wheel retains a PC-type wear pattern throughout the simulated service life, with its nominal peak remaining close to the nominal tread center and showing no substantial outward migration. Overall, for the same service mileage, the nominal peak of the B-type locomotive wheel lies closer to the flange side, indicating that its tread geometry and loading conditions are more sensitive to lateral peak migration.

Fig. 19 shows the equivalent conicity of the worn wheels in combination with CN60 and CN60N rails after long-distance wear. Fig. 19(a and b) give the results for the B-type locomotive wheel in combination with CN60 and CN60N, respectively, while Fig. 19(c and d) present the corresponding results for the C-type locomotive wheel. Each subfigure includes results for rail inclination values of 1:35, 1:40 and 1:45, which are distinguished by color; mileage is not differentiated by color.

From Fig. 19 it can be observed that equivalent conicity is markedly lower than that of the combination with CN60 rails when the worn wheels are in combination with CN60N rails. This trend is consistent with the results for measured wheel profiles shown in Fig. 3(e and f).

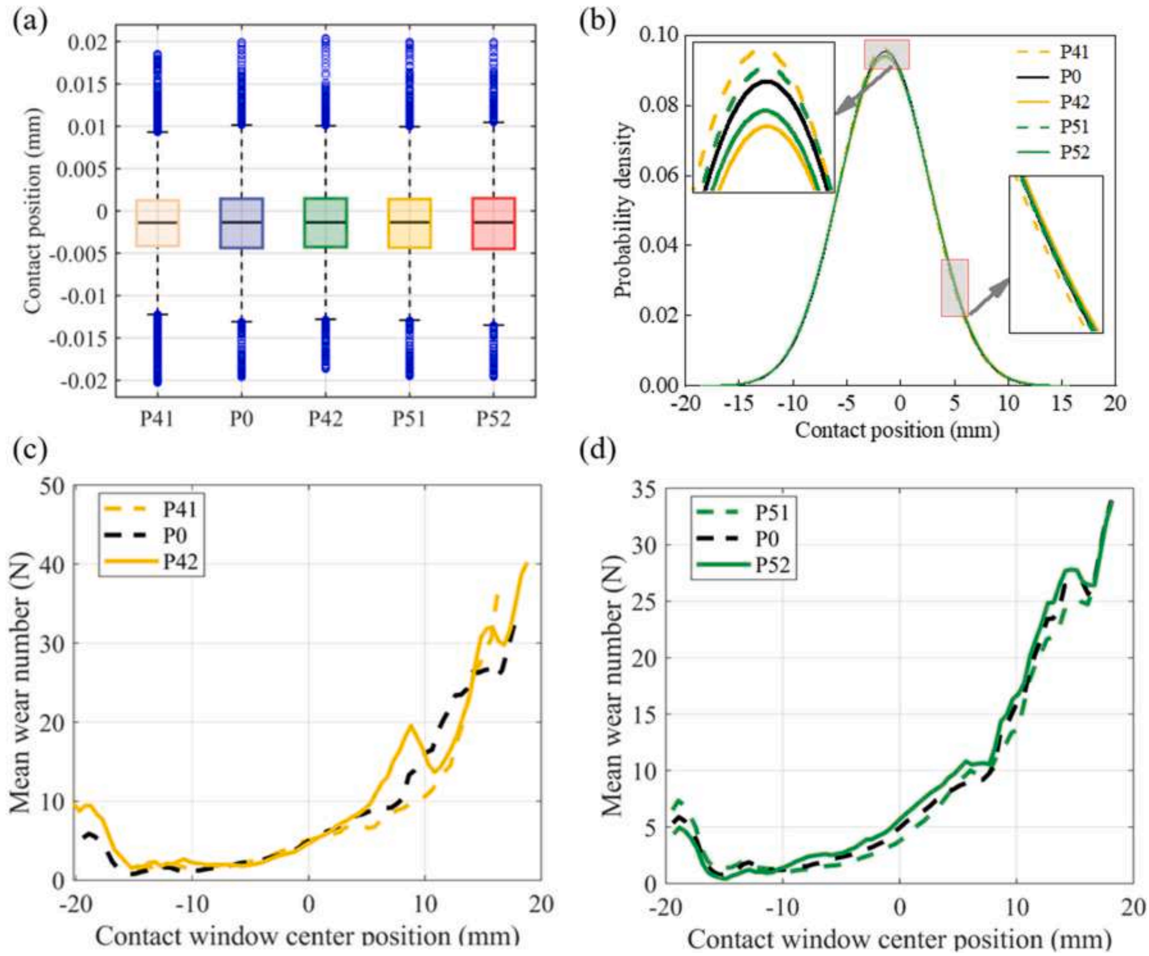

Fig. 17. Distribution of contact point locations and wear metrics under different running speeds and axle torques: (a) Boxplots of contact point position; (b) Probability density functions of contact point position; (c) Mean wear number versus contact window center, speed cases; (d) Mean wear number versus contact window center, axle-torque cases.

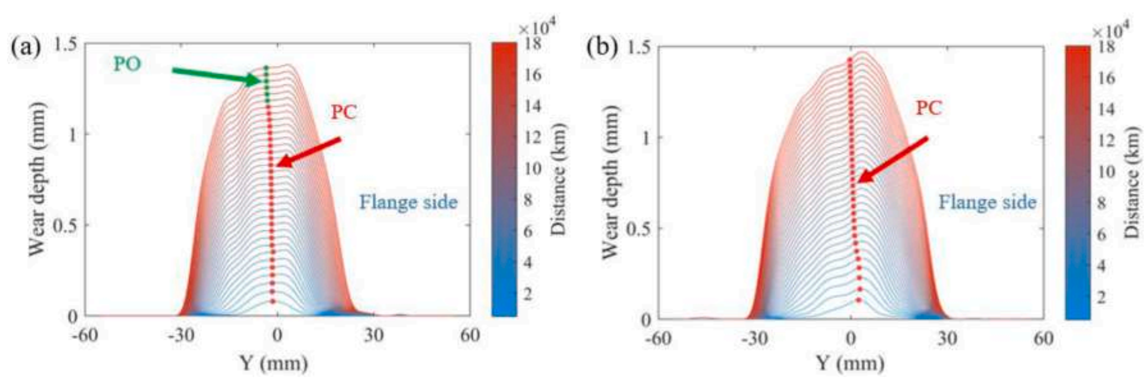

Fig. 18. Long-distance wheel wear distribution for B-type and C-type locomotives under the baseline parameter set (P0). (a) B-type locomotive; (b) C-type locomotive.

Furthermore, a higher rail inclination (for example 1:35) corresponds to lower conicity. Fig. 19(a–c) show that, when in combination with CN60 rails, the equivalent conicity of the B-type worn wheels is substantially greater than that of the C-type locomotive wheels and is relatively insensitive to rail inclination variation. Combined inspection of Figs. 18 and 19 suggests that, in the mid-to-late stages of wear, the evolution of equivalent conicity is affected more by the lateral migration of the nominal wear peak than by the absolute wear depth.

4.4.2. Track conditions and driving requirements

Fig. 20(a–d) presents the evolution of the nominal wear-peak location and wear depth for B-type and C-type locomotives under different combinations of track conditions and driving requirement parameters. Fig. 20(a and b) corresponds to the B-type locomotive, while Fig. 20(c and d) corresponds to the C-type locomotive.

From Fig. 20(a–c), both locomotive types exhibit an overall outward migration of the nominal peak position as mileage increases. For the B-type locomotive, the initial peak is generally located between −2 mm

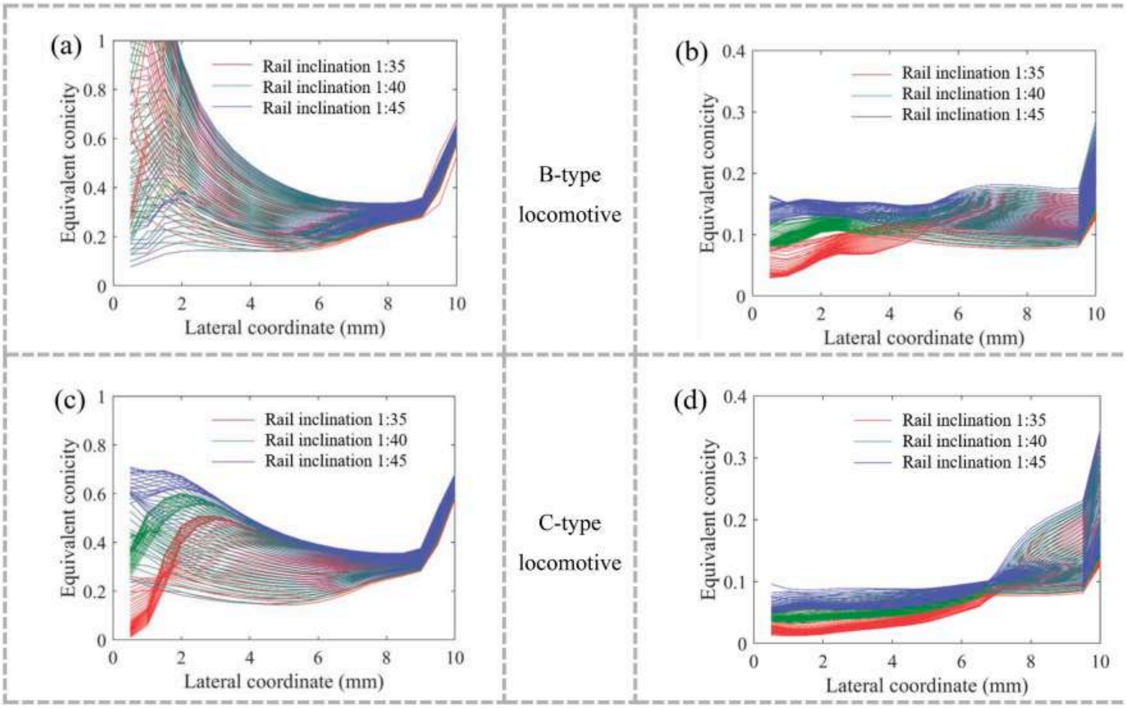

Fig. 19. Equivalent conicity of worn wheels for B-type and C-type locomotives in combination with CN60 and CN60N rails (Results include rail inclination values of 1:35, 1:40, and 1:45).

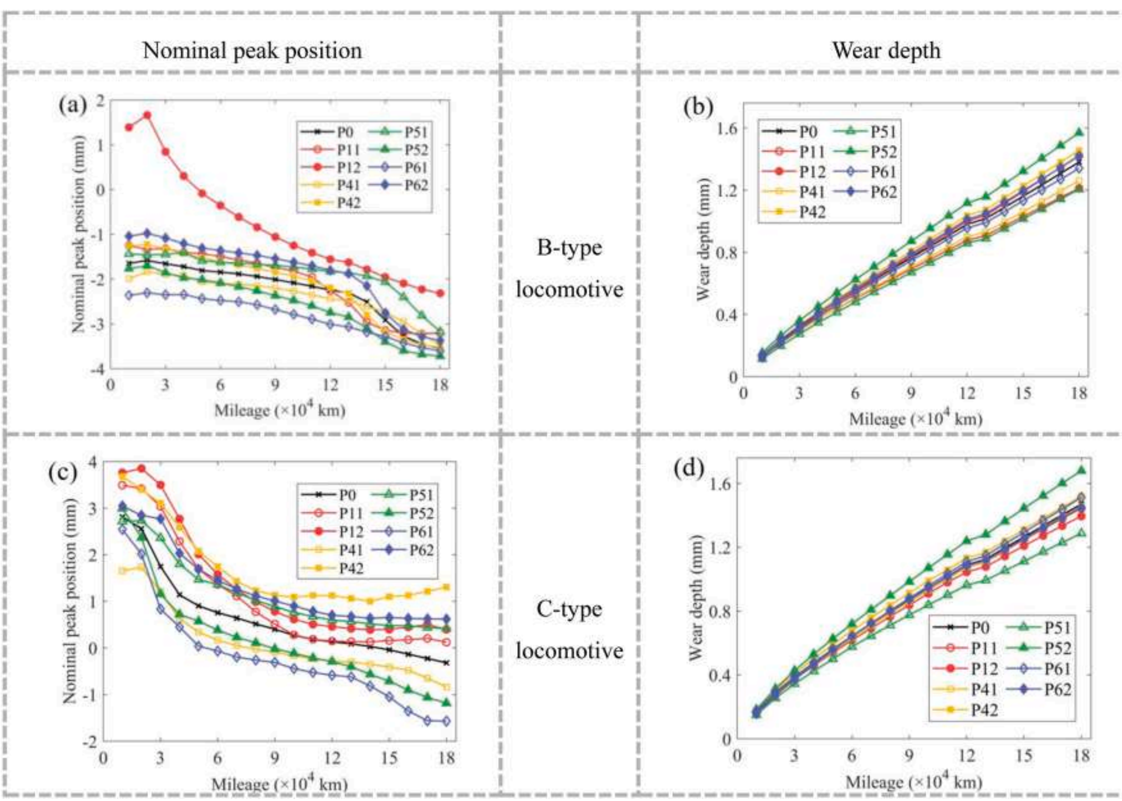

Fig. 20. Evolution of nominal wear-peak position and wear depth under different parameter combinations.

and −1 mm. When the mileage reaches approximately 120,000 km, certain parameter combinations, such as P61 (corresponding to a steeper rail inclination), cause the peak to shift to about −3 mm, indicating a transition to PO-type wear. For the C-type locomotive, the initial nominal peak is located near 3 mm. In cases such as P11, P12 and P42, where the percentage of CN60 rails is increased or the operating speed is higher, the peak shifts further toward the flange side, leading to PF-type wear. As mileage approaches 100,000 km, the peak position moves toward the nominal tread center, after which its progression becomes relatively slow.

The evolution of wear depth is shown in Fig. 20(b–d). Axle torque is the most influential parameter affecting wear-depth growth. Higher axle torque significantly accelerates wear development. Increasing the percentage of CN60 rails reduces the wear rate, as the combination with CN60 rails provides a more uniform contact point distribution (see Fig. 16), which mitigates concentrated material loss. For the C-type locomotive, for example, a 10% reduction in axle torque results in the same wear depth at 180,000 km as that observed at approximately 150,000 km before the axle torque reduction, indicating a substantial mitigating effect.

Figs. 21 and 22 show the tread wear conditions of the two locomotives after 180,000 km of service under various parameter combinations. The influence trends of each factor on the wear distribution are consistent with the analyses in Fig. 20, which further confirms the validity of using the nominal peak of the wear distribution, as proposed in Section 2, to classify worn wheels.

Fig. 23 shows the equivalent conicity at 180,000 km for worn wheels in combination with CN60 and CN60N rails. Fig. 23(a and b) corresponds to the B-type locomotive, and Fig. 23(c and d) to the C-type locomotive. From Fig. 23(a) and (b), it can be observed that the equivalent conicity of the worn wheels generated under different simulation conditions for the B-type locomotive shows only minor variation. This indicates that when the nominal peak shifts outward, that is, farther away from the nominal tread center, the equivalent conicity becomes relatively insensitive to further changes in the peak position. In contrast, Fig. 23(c) shows that the equivalent conicity of the C-type locomotive varies substantially under different simulation conditions, suggesting that the findings of this study are particularly effective for guiding wheel maintenance of the C-type locomotive.

By examining the results presented in Fig. 21 through Fig. 23, it can be concluded that combinations of parameters that induce outward migration of the nominal peak generally result in higher equivalent conicity, whereas combinations that promote inward peak shifting tend to reduce equivalent conicity. These observations further demonstrate that, in the mid-to-late stages of wear, equivalent conicity is affected more by the lateral migration of the nominal peak than by the absolute wear depth.

To clarify the progression of equivalent conicity at multiple mileages for the C-type locomotive in combination with CN60 rails, Fig. 24 presents three-dimensional views of equivalent conicity across lateral wheel position and mileage for selected parameter groups. In each subfigure the x-axis is the lateral wheel position, the y-axis is mileage, and the z-axis is equivalent conicity.

Fig. 24 results indicate that equivalent conicity changes little at the very early stage. As mileage increases, notable divergence in conicity emerges within the lateral displacement range of less than 4 mm. Specifically, an increased CN60 proportion, higher running speed, and reduced axle torque all slow the rate of conicity increase; this behaviour is consistent with the observed trends of nominal-peak migration. As a supplementary remark, although rail inclination strongly affects the nominal peak position, the conicity calculation for a given worn wheel uses the rail inclination corresponding to the rail that generated that wheel profile. As shown in Fig. 19(c), for the same wheel tread the selected rail inclination can significantly alter the computed conicity; therefore, conicity differences between wheels generated under varying inclination values may be small when each conicity is evaluated with its generating cant. In practice, rail inclination varies within a range along a route, and this variability should be considered when interpreting conicity results.

In summary, track geometry and driver-controllable operating parameters jointly determine the long-term lateral migration of the nominal wear peak and the evolution of equivalent conicity. Axle torque predominantly controls wear-rate growth, while CN60 proportion, running speed and rail inclination modulate the lateral migration and hence the conicity trajectory in the middle to late wear stages.

5. Summary and outlook

In this study, the long-term tracking measurements of locomotive wheel wear were systematically processed and analyzed, and worn wheel profiles were classified according to the nominal peak position of the wear distribution. Using the B-type and C-type locomotives as case studies, a long-distance iterative wear prediction model was developed to analyze in-service wear evolution. The effects of the dominant factors, including rail profile, operating speed, axle torque, and rail inclination, on tread wear evolution were systematically investigated. The principal

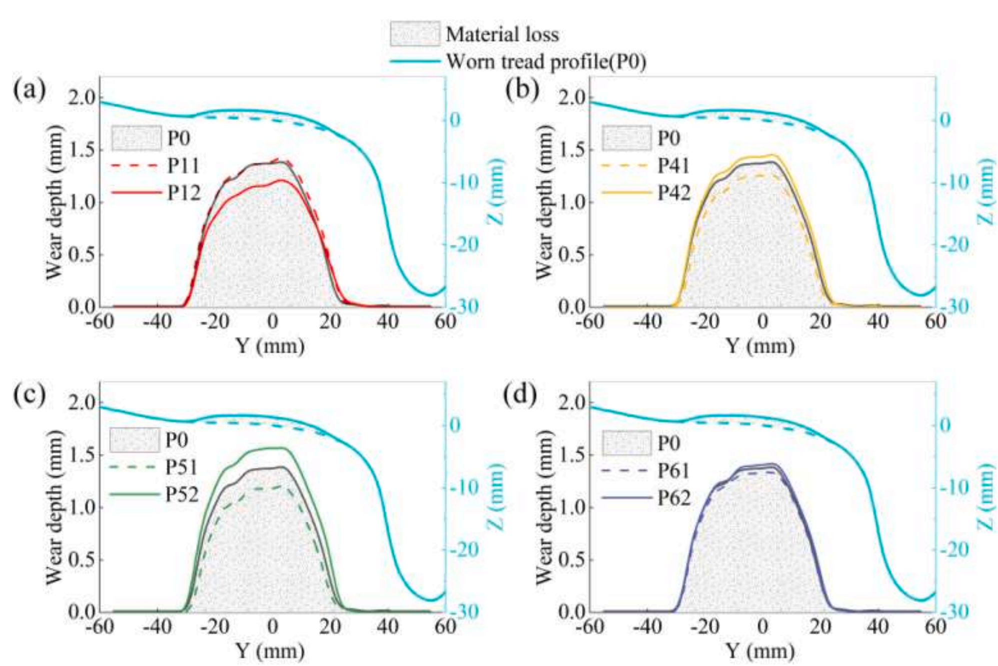

Fig. 21. The tread wear condition of the B-type locomotive after 180,000 km of service under different parameter combinations.

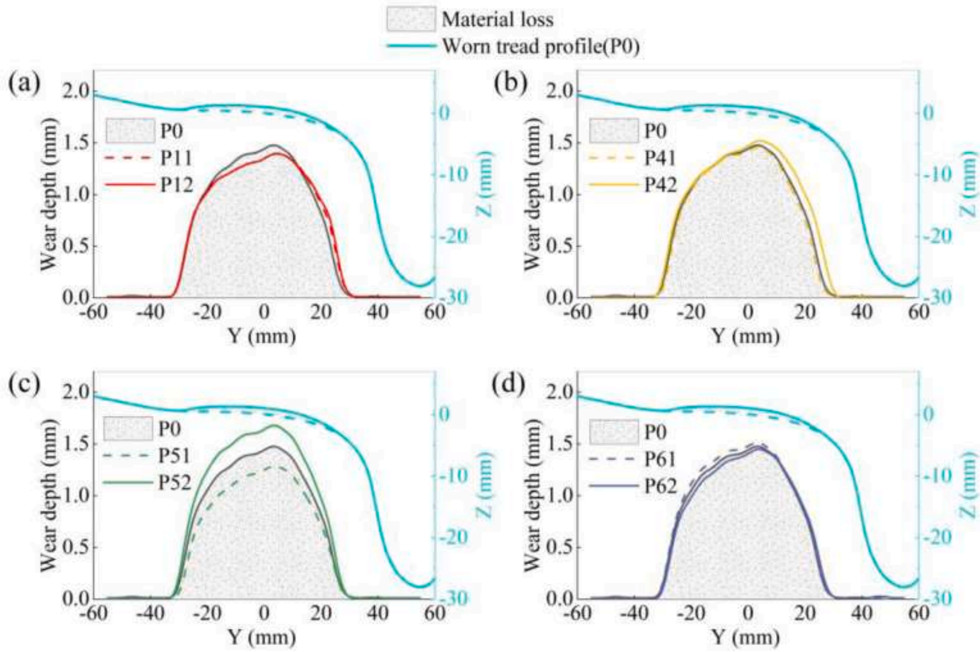

Fig. 22. The tread wear condition of the C-type locomotive after 180,000 km of service under different parameter combinations.

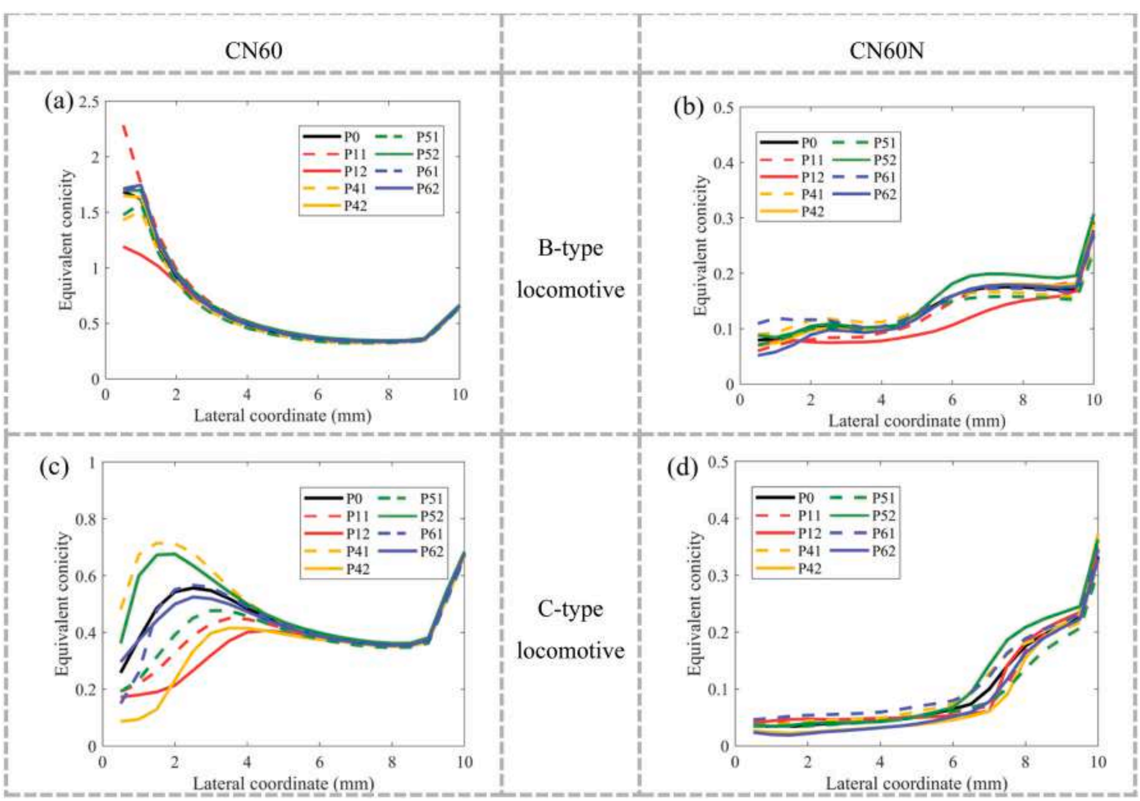

Fig. 23. Equivalent conicity of worn wheels at 180,000 km under different simulation conditions.

findings include.

(1) The nominal peak position of the wear distribution provides an effective basis for classifying worn wheels and capturing the characteristic differences among tread wear modes. This classification method enables clear interpretation of how different wear morphologies influence equivalent conicity.

(2) For the C-type locomotive, the evolution of equivalent conicity is affected more by the lateral migration of the nominal wear peak than by the absolute wear depth. This highlights the dominant role of wear distribution, rather than mere wear magnitude, in determining wheel–rail contact geometry during long-term service. Increasing the percentage of CN60 rail, increasing operating speed, and reducing axle torque all contribute to mitigating

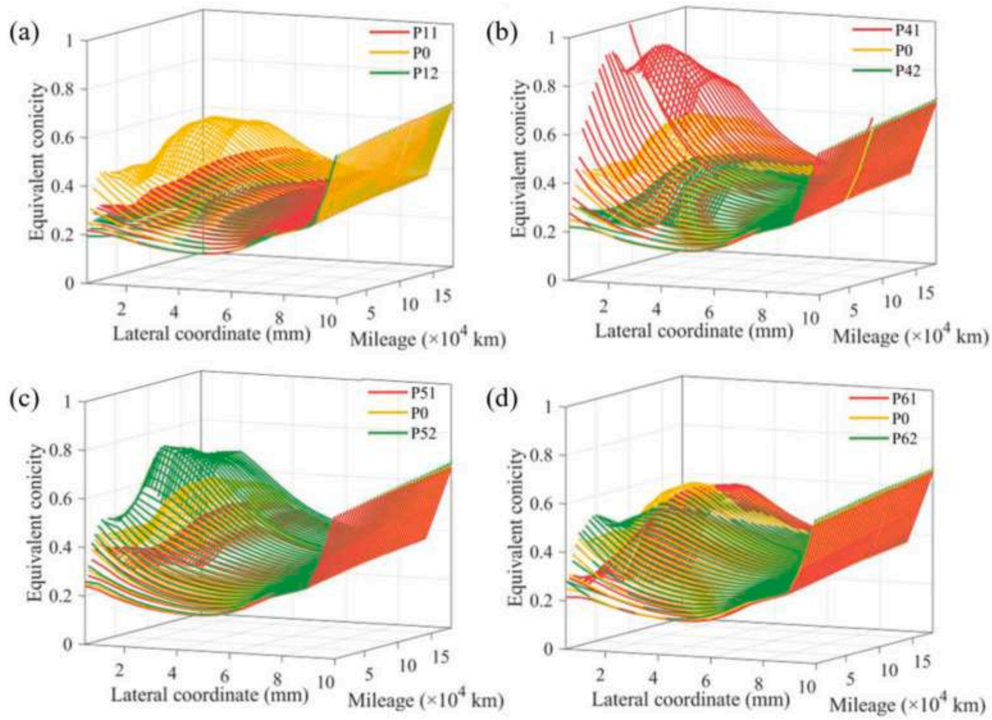

Fig. 24. Evolution of equivalent conicity for C-type worn wheels in combination with CN60 rail.

equivalent conicity growth. As long as the conicity remains within its allowable range, the reprofiling interval may be appropriately extended to improve wheel life, thereby improving wheel life, reducing maintenance frequency, and enhancing the economic efficiency of locomotive operation.

(3) The factors analyzed in this study induce only minor variations in the equivalent conicity of the B-type locomotive, indicating that once the nominal wear peak has migrated outward from the nominal tread center, equivalent conicity becomes relatively insensitive to further changes in peak position. Therefore, wheel maintenance for the B-type locomotive should focus primarily on controlling wear depth.

(4) More generally, the evolution of wheel wear and contact geometry is strongly influenced by the spatial distribution of contact points. A contact geometry characterized by a more uniform contact-point distribution, such as that associated with CN60 rails, is less vulnerable to rapid profile alteration, whereas a more concentrated contact distribution in narrow zones, such as that associated with CN60N rails, tends to promote localized wear accumulation and faster equivalent-conicity growth.

The findings of this study provide theoretical support for condition-based and predictive wheel maintenance in power-concentrated locomotives. The proposed classification framework and wear prediction model can be directly applied to intelligent wheel–rail health management systems. In practical application, wheel and rail profiles, together with relevant operating or dynamic-response data, can be periodically collected to assess the current wheel–rail contact geometry using indicators such as equivalent conicity and wear distribution. The proposed model can then be used to predict the future evolution of these indicators and support maintenance decisions, such as extending the reprofiling interval when the predicted condition remains within allowable limits or scheduling earlier intervention when the limits are approached.

CRediT authorship contribution statement

Hu Li: Conceptualization, Formal analysis, Methodology, Software, Validation, Writing – original draft. **Yuan Yao:** Funding acquisition, Software, Supervision. **Zhiyong Shi:** Funding acquisition, Writing – review & editing. **Enrico Meli:** Methodology, Supervision. **Xiaoxing Deng:** Data curation, Validation. **Jijun Gong:** Data curation, Validation. **Guang Li:** Funding acquisition, Software.

Declaration of competing interest

The authors declare that they have no known competing financial interests or personal relationships that could have appeared to influence the work reported in this paper.

Acknowledgments

This work was supported by the National Natural Science Foundation of China [grant number 52372403], the National Railway Group Science and Technology Program [grant numbers N2025J026; Q2024J013], the State Key Laboratory of Rail Transit Vehicle System [grant number RVLHW202404], and Research Project of China Academy of Railway Sciences Group Co., Ltd [grant number 2025YJ010].

Data availability

Data will be made available on request.

References

[1] J. Liu, P. Chen, Y. Ou, G. Zhou, P. Yu, Z. Xu, et al., Study on wear and rolling contact damage mechanism between quenched U75V rail and wheels with different microstructures, Wear 512–513 (2023) 204544, https://doi.org/10.1016/j.wear.2022.204544.

[2] T. Zhu, H. Zhang, W. Wang, Q. Lin, Z.F. Wen, H. Ding, et al., Experimental study on the influence of slip ratio on irregular wear behaviors of wheel/rail, Wear 523 (2023) 204780, https://doi.org/10.1016/j.wear.2023.204780.

[3] H. Li, L. Li, X. Yu, Z. Li, Y. Sun, Research on the influence of time-varying wear of wheel-rail profile on vehicle dynamic response, Tribol. Int. 200 (2024) 110095, https://doi.org/10.1016/j.triboint.2024.110095.
[4] Y. Xie, M. Chi, W. Cai, S. Liang, Y. Li, Y. Zhou, et al., A framework for wheel profile wear prediction of high-speed trains considering tread modification, Friction 13 (2025) 9441060, https://doi.org/10.26599/FRICT.2025.9441060.
[5] N. Bosso, M. Magelli, N. Zampieri, Simulation of wheel and rail profile wear: a review of numerical models, Rail Eng Sci 30 (2022) 403–436, https://doi.org/10.1007/s40534-022-00279-w.
[6] B. Wen, S. Wang, G. Tao, J. Li, D. Ren, et al., Prediction of rail profile evolution on metro curved tracks: wear model and validation, Int J Rail Transp 11 (6) (2023) 811–832, https://doi.org/10.1080/23248378.2022.2113923.
[7] R. Luo, B. Liu, S. Qu, A fast simulation algorithm for the wheel profile wear of high-speed trains considering stochastic parameters, Wear 480–481 (2021) 203942, https://doi.org/10.1016/j.wear.2021.203942.
[8] L. Nencioni, E. Meli, A. Rindi, Z. Shi, A new efficient conformal contact model for multibody and railway applications, Multibody Syst. Dyn. 64 (2025) 587–626, https://doi.org/10.1007/s11044-024-10028-y.
[9] I.S. Apezetxea, X. Perez, A. Alonso, Experimental validation of a fast wheel wear prediction model, Wear 486–487 (2021) 204090, https://doi.org/10.1016/j.wear.2021.204090.
[10] S. H-Nia, J. Flodin, C. Casanueva, M. Asplund, S. Stichel, Predictive maintenance in railway systems: MBS-Based wheel and rail life prediction exemplified for the Swedish iron-ore line, Veh. Syst. Dyn. 62 (1) (2024) 3–20, https://doi.org/10.1080/00423114.2022.2161920.
[11] S. H-Nia, V.V. Krishna, K. Odolinski, P.T. Torstensson, A. Ait-Ali, L. Sundholm, et al., Simulation-based evaluation of maintenance strategies from a life cycle cost perspective, Wear 532–533 (2023) 205120, https://doi.org/10.1016/j.wear.2023.205120.
[12] S. Liu, Q. He, W. Fu, Q. Feng, A two-step data-driven method for predicting the wear of train wheel treads using GA-BPNN and LSTM algorithms, Int J Rail Transp 13 (1) (2025) 85–102, https://doi.org/10.1080/23248378.2024.2324092.
[13] M. Wang, S. Jia, E. Chen, S. Yang, P. Liu, Z. Qi, Research and application of neural network for tread wear prediction and optimization, Mech. Syst. Signal Process. 162 (2022) 108070, https://doi.org/10.1016/j.ymssp.2021.108070.
[14] C. Chen, F. Zhu, Z. Xu, Q. Xie, S.M. Lo, K.L. Tsui, et al., Knowledge-informed wheel wear prediction method for high-speed train using multisource signal data, IEEE Trans. Instrum. Meas. 73 (2024) 1–12, https://doi.org/10.1109/TIM.2024.3413151.
[15] B. Liu, S. Bruni, Influence of individual wheel profiles on the assessment of running dynamics of a rail vehicle by numerical simulation: a case study, Veh. Syst. Dyn. 60 (7) (2022) 2393–2412, https://doi.org/10.1080/00423114.2021.1901940.
[16] H. Li, T. Tan, S. Stichel, Y. Yao, Investigating hunting stability failure in a high-speed locomotive: a comparative analysis of evaluation methods for typical worn wheel treads, Eng. Fail. Anal. 174 (2025) 109482, https://doi.org/10.1016/j.engfailanal.2025.109482.
[17] R. Kulkarni, A. Qazizadeh, M. Berg, B. Dirks, I. Persson, Investigating the effect of the equivalent conicity function's nonlinearity on the dynamic behaviour of a rail vehicle under typical service conditions, Veh. Syst. Dyn. 60 (10) (2022) 3484–3503, https://doi.org/10.1080/00423114.2021.1962537.
[18] B. Firlik, T. Staśkiewicz, W. Jaśkowski, L. Wittenbeck, Optimisation of a tram wheel profile using a biologically inspired algorithm, Wear 430–431 (2019) 12–24, https://doi.org/10.1016/j.wear.2019.04.012.
[19] Y. Ye, Y. Qi, D. Shi, Y. Sun, Y. Zhou, M. Hecht, Rotary-scaling fine-tuning (RSFT) method for optimizing railway wheel profiles and its application to a locomotive, Rail Eng Sci 28 (2) (2020) 160–183, https://doi.org/10.1007/s40534-020-00212-z.
[20] Y. Qi, H. Dai, F. Gan, H. Gao, Optimisation of wheel profile of variable gauge high-speed trains, Veh. Syst. Dyn. 62 (3) (2024) 651–672, https://doi.org/10.1080/00423114.2023.2186250.
[21] H. Li, Y. Yao, X. Chen, Suspension parameter optimization for high-speed train with severe tread wear, Int J Rail Transp 13 (2) (2025) 381–401, https://doi.org/10.1080/23248378.2024.2345683.
[22] Y. Song, Y. Qi, H. Dai, Multi-parameter optimization based on a surrogate model for improving vehicle dynamics and reducing wheel wear in high-speed EMUs, Veh. Syst. Dyn. (2024) 1–24, https://doi.org/10.1080/00423114.2024.2430577.
[23] G. Li, R. Wu, X. Deng, L. Shen, Y. Yao, Suspension parameters matching of high-speed locomotive based on stability/comfort pareto optimization, Veh. Syst. Dyn. 60 (11) (2022) 3848–3867, https://doi.org/10.1080/00423114.2021.1979602.
[24] X. Zhang, H. Li, J. Cheng, L. Sheng, Y. Yao, Adaptive stability mechanism of high-speed train employing parallel inerter yaw damper, Veh. Syst. Dyn. 61 (1) (2023) 38–57, https://doi.org/10.1080/00423114.2022.2045027.
[25] S. Stichel, R. Persson, R. Giossi, Improving rail vehicle dynamic performance with active suspension, High-Speed Rail 1 (1) (2023) 23–30, https://doi.org/10.1016/j.hspr.2022.12.002.
[26] M. Hou, B. Chen, D. Cheng, Study on the evolution of wheel wear and its impact on vehicle dynamics of high-speed trains, Coatings 12 (9) (2022) 1333, https://doi.org/10.3390/coatings12091333.
[27] B. Zheng, L. Wei, J. Zeng, C. Huang, Carbody hunting behaviour of high speed vehicles in low effective conicity of wheel-rail contact, Proc. Inst. Mech. Eng. F J. Rail Rapid Transit 238 (9) (2024) 1108–1120, https://doi.org/10.1177/09544097241262395.
[28] Z. Wang, D. Gong, A survey on countermeasures of railway vehicle stability decrease caused by the evolution of hollow-worn wheels, J. Vib. Control 31 (5–6) (2024) 864–877, https://doi.org/10.1177/10775463241234726.
[29] Y. Qi, H. Dai, Y. Song, F. Zhang, S. Lu, Research on the characteristics of wheel hollow wear and suppression measures of high-speed trains, Tribol. Trans. 66 (4) (2023) 597–609, https://doi.org/10.1080/10402004.2023.2191659.
[30] C. Chang, X. Ding, L. Ling, F. Li, T. Liu, K. Wang, et al., Mechanism of high-speed train carbody shaking due to degradation of wheel-rail contact geometry, Int J Rail Transp 11 (3) (2023) 289–316, https://doi.org/10.1080/23248378.2022.2077850.
[31] M.C. Burstow, A model to predict and understand rolling contact fatigue in wheels and rails, in: Proceedings of the 7th World Congress on Railway Research (WCRR 2006), 2006 Jun 4–8. Montreal, Canada.
[32] J. Sun, M. Chi, X. Jin, S. Liang, J. Wang, W. Li, Experimental and numerical study on carbody hunting of electric locomotive induced by low wheel–rail contact conicity, Veh. Syst. Dyn. 59 (2) (2021) 203–223, https://doi.org/10.1080/00423114.2019.1674344.
[33] Y. Yao, X. Chen, H. Li, G. Li, Suspension parameters design for robust and adaptive lateral stability of high-speed train, Veh. Syst. Dyn. 61 (4) (2023) 943–967, https://doi.org/10.1080/00423114.2022.2062012.
[34] O. Polach, Characteristic parameters of nonlinear wheel/rail contact geometry, Veh. Syst. Dyn. 48 (sup1) (2010) 19–36, https://doi.org/10.1080/00423111003668203.
[35] G. Tao, X. Du, H. Zhang, Z. Wen, X. Jin, D. Cui, Development and validation of a model for predicting wheel wear in high-speed trains, J. Zhejiang Univ. - Sci. 18 (2017) 603–616, https://doi.org/10.1631/jzus.A1600693.
[36] J. Piotrowski, H. Chollet, Wheel-rail contact models for vehicle system dynamics including Non-Hertzian contact, Veh. Syst. Dyn. 43 (6–7) (2005) 455–483, https://doi.org/10.1080/00423110500141144.
[37] B. Liu, S. Bruni, R. Lewis, Numerical calculation of wear in rolling contact based on the archard equation: effect of contact parameters and consideration of uncertainties, Wear 490–491 (2022) 204188, https://doi.org/10.1016/j.wear.2021.204188.
[38] J.J. Kalker, A fast algorithm for the simplified theory of rolling contact, Veh. Syst. Dyn. 11 (1) (1982) 1–13, https://doi.org/10.1080/00423118208968684.
[39] R. Lewis, U. Olofsson, Mapping rail wear regimes and transitions, Wear 257 (7–8) (2004) 721–729, https://doi.org/10.1016/j.wear.2004.03.019.
[40] F. Braghin, R. Lewis, R.S. Dwyer-Joyce, S. Bruni, A mathematical model to predict railway wheel profile evolution due to wear, Wear 261 (11–12) (2006) 1253–1264, https://doi.org/10.1016/j.wear.2006.03.025.
[41] H. Ding, C.G. He, L. Ma, J. Guo, Q.Y. Liu, W.J. Wang, Wear mapping and transitions in wheel and rail materials under different contact pressure and sliding velocity conditions, Wear 352–353 (2016) 1–8, https://doi.org/10.1016/j.wear.2016.01.017.
[42] Z. Shi, L. Nencioni, E. Meli, H. Ding, W. Wang, A. Rindi, Effect of material hardness ratio on wear and rolling contact fatigue: development and validation of new laws, Wear 514–515 (2023) 204561, https://doi.org/10.1016/j.wear.2022.204561.
[43] B. Yang, L. Guo, J. Guo, W. Wang, Q. Liu, Simulation analysis of wheel wear based on the model of $T\gamma/A$ wear rate, J. Mech. Eng. 53 (22) (2017) 101–108, https://doi.org/10.3901/JME.2017.22.101.
[44] P.J. Bolton, P. Clayton, Rolling–sliding wear damage in rail and tyre steels, Wear 93 (2) (1984) 145–165, https://doi.org/10.1016/0043-1648(84)90066-8.
[45] H. Gao, H. Dai, Wheel-rail contact point calculation of flexible wheelset base on wheel-rail contact line method, Appl. Mech. Mater. 105–107 (2012) 1284–1288. https://dx.doi.org/10.4028/www.scientific.net/AMM.105-107.1284.
[46] J.B. Ayasse, H. Chollet, Determination of the wheel rail contact patch in semi-hertzian conditions, Veh. Syst. Dyn. 43 (3) (2005) 161–172, https://doi.org/10.1080/00423110412331327193.
[47] J. Piotrowski, W. Kik, A simplified model of wheel/rail contact mechanics for Non-Hertzian problems and its application in rail vehicle dynamic simulations, Veh. Syst. Dyn. 46 (1–2) (2008) 27–48, https://doi.org/10.1080/00423110701586444.
[48] H. Magalhães, F. Marques, B. Liu, P. Antunes, J. Pombo, P. Flores, et al., Implementation of a Non-Hertzian contact model for railway dynamic application, Multibody Syst. Dyn. 51 (2021) 41–78, https://doi.org/10.1007/s11044-020-09755-y.